Z. Physik C, Particles and Fields 3, 101–123 (1979)

Zeitschrift für Physik C Particles and Fields

Electroproduction of $\pi^+ n$, $\pi^- p$ and $K^+ \Lambda$, $K^+ \Sigma^0$ Final States Above the Resonance Region

P. Brauel, T. Canzler, D. Cords, R. Felst, G. Grindhammer*, M. Helm, W.-D. Kollmann, H. Krehbiel, and M. Schädlich**

Deutsches Elektronen-Synchrotron DESY, D-2000 Hamburg 52, Federal Republic of Germany, and
II. Institut für Experimentalphysik der Universität Hamburg, Federal Republic of Germany

Received 18 September 1979

Abstract: The reactions $\gamma_v p \to \pi^+ n$, $K^+\Lambda$, $K^+\Sigma^0$ and $\gamma_v n \to \pi^- p$ were studied at invariant hadronic masses around 2.2 GeV for $Q^2 = 0.06$, 0.28, 0.70, and 1.35 GeV^2. The main results are: At small $|t|$ the π^+ production is dominated by longitudinally polarized photons and can be described by one pion exchange. At low $|t|$ the transverse $(\pi^+ n)$ cross section drops steeply with Q^2, but remains roughly constant for $Q^2 \geqq 0.5$ GeV^2. For $|t| \geqq 0.8$ GeV^2, $d\sigma(\pi^+ n)/dt$ is almost independent of Q^2. The integrated cross section $\sigma(\pi^+ n)$ shows a similar Q^2-dependence as $\sigma_{\text{tot}}(\gamma_v p)$ for $Q^2 \geqq 0.28$ GeV^2. The ratio $\sigma(\pi^- p)/\sigma(\pi^+ n)$ at $Q^2 = 0.70$ and 1.35 GeV^2 for $|t| \geqq 0.6$ GeV^2 is smaller than in photoproduction and close to 1/4. The ratio $\sigma(K^+\Sigma^0)/\sigma(K^+\Lambda)$ decreases steeply with Q^2 following roughly the predictions of the quark-parton model.

1. Introduction

This article presents the results of an experiment on $\pi^\pm$ and K^+ electroproduction above the resonance region. Parts of the $\pi^\pm$ data have been previously reported [1–3].

This experiment was initiated in 1972, when the scaling behaviour of deep inelastic electron scattering was well established but only little was known about the behaviour of exclusive channels. The forward vector meson production $\gamma_v + p \to p + \rho^0, \omega$ showed diffractive behaviour [4], the integrated cross section $\sigma(\gamma_v + p \to \rho^0 + p)$ dropping faster with increasing Q^2 than the total cross section $\sigma(\gamma_v p)$. Measurements of small angle single pion electroproduction $\gamma_v + p \to \pi^+ + n$ showed indication [5] of dominating contribution from longitudinally polarized photons. This longitudinal cross section could be explained by the one pion exchange contribution in the electric Born term model [6, 7]. Since these two channels measured then were dominated by peripheral production mechanisms, one would not expect to see effects of the short range interaction which was postulated in the parton model to explain the approximate scaling behaviour of $\sigma_{\text{tot}}(\gamma_v p)$. However, a more detailed analysis [6] of the $\gamma_v + p \to \pi^+ + n$ data indicated that the transverse cross section might show a slow decrease with Q^2 similar to $\sigma_{\text{tot}}(\gamma_v p)$.

One would expect to find possible evidence for the short range interaction picture in exclusive channels at large values of the virtual photon mass Q^2 and of the nucleon momentum transfer $|t|$. In this kinematic region cross sections are small, therefore to pursue such studies the experimentally easily accessible channel $\gamma_v + p \to \pi^+ + n$ was chosen. Specifically our aims were:

a) to separate the longitudinal and transverse cross sections,
b) to extend the measurements to larger values of Q^2 and $|t|$, and
c) to study the isospin structure of the contributing amplitudes by measuring in addition the reaction $\gamma_v + n \to \pi^- + p$.

Since kaons were detected simultaneously with the pions, we also studied the reactions $\gamma_v + p \to K^+ + \Lambda$, $K^+ + \Sigma^0$ in some detail.

The outline of the paper is the following: In Sect. 2 the kinematical variables and cross sections are defined, in Sect. 3 a short description of the experimental procedure is given. The results of the data analysis are presented in Sect. 4. A discussion of the results and a comparison with other experiments as well as certain model predictions are given in Sect. 5. Section 6 contains a summary.

* Now at Max-Planck-Institut für Physik und Astrophysik, D-8000 München

** Now at Alfried Krupp v. Bohlen und Halbach Stiftung, D-4300 Essen

0170-9739/79/0003/0101/$04.60

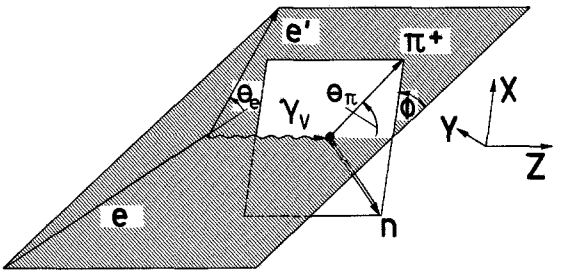

Fig. 1. The reaction $e+p\to e'+\pi^+ +n$ in the laboratory system

2. Kinematics, Cross Sections, and Radiative Corrections

The definition of the kinematical variables, which are sketched in Fig. 1, is exemplified by the reaction $e+p\to e'+n+\pi^+$. The five four-momenta involved are:

$e=(E,\mathbf{e})$ incident electron
$e'=(E',\mathbf{e}')$ scattered electron
$p=(M,\mathbf{0})$ target nucleon
$\pi=(E_\pi,\boldsymbol{\pi})$ produced meson
$n=(E_n,\mathbf{n})$ final baryon.

The only four-momentum not measured directly in this experiment is n. The emitted baryon is identified by its missing mass $M_n^2=(e-e'+p-\pi)^2$.

The reaction is described to lowest order by the exchange of a virtual photon γ_v; higher order effects are contained in the radiative corrections. The following Lorentz invariants are commonly used to define the kinematics:

$$\gamma_v^2=(e-e')^2=-Q^2$$
$$s=(\gamma_v+p)^2=W^2$$
$$t=(\gamma_v-\pi)^2.$$

The incident particles are unpolarized and no polarization is measured of the final particles. However the exchanged photon is polarized. Its polarization is described by a parameter ε, which is equal to the transverse linear polarization and closely related to the longitudinal polarization:

$$\varepsilon=\frac{|A_x|^2-|A_y|^2}{|A_x|^2+|A_y|^2}=\left[1+2\,\frac{Q^2+(E-E')^2}{Q^2}\,\mathrm{tg}^2\,\frac{\theta_e}{2}\right]^{-1}$$
$$\frac{|A_z|^2}{|A_x|^2+|A_y|^2}=\frac{Q^2}{(E-E')^2}\cdot\varepsilon. \tag{2.1}$$

We write the differential cross section as (for a summary of various conventions see [7]):

$$\frac{d^4\sigma}{dQ^2 ds dt d\phi}=\Gamma\cdot 2\pi\cdot\frac{d^2\sigma}{dt d\phi} \tag{2.2}$$

The virtual photon flux Γ is given by

$$\Gamma=\frac{\alpha(s-M^2)}{(4\pi)^2E^2M^2Q^2}\cdot\frac{1}{(1-\varepsilon)} \tag{2.3}$$

and the cross section for single hadron production by virtual photons is written as

$$2\pi\frac{d^2\sigma}{dt d\phi}=\frac{d\sigma_U}{dt}+\varepsilon\frac{d\sigma_L}{dt}+\varepsilon\frac{d\sigma_P}{dt}\cos 2\phi$$
$$+\sqrt{2\varepsilon(\varepsilon+1)}\,\frac{d\sigma_I}{dt}\cos\phi. \tag{2.4}$$

ϕ is the angle between the hadron production plane and the electron scattering plane as defined in Fig. 1. $\sigma_U=\frac{1}{2}(\sigma_{\|}+\sigma_\perp)$ is the contribution from transversely unpolarized photons, $\sigma_P=\frac{1}{2}(\sigma_{\|}-\sigma_\perp)$ from the interference of the transversely polarized photons, σ_L from longitudinally polarized photons, and σ_I from the interference of transversely and longitudinally polarized photons. $\sigma_{\|}$ and $\sigma_\perp$ are the cross sections for photons having the electric vector parallel and perpendicular to the hadron production plane, respectively. The four different cross sections can be separated by measuring the ϕ and ε dependence of (2.4).

At high s the cross sections $\sigma_\perp$, $\sigma_{//}$, σ_L, and σ_I are characterized by a unique naturality of the t-channel exchange [8]. Natural parity exchange contributes only to $\sigma_\perp$ and unnatural parity exchange only to $\sigma_{\|}$, σ_L, and σ_I.

Higher order effects to the cross section (2.2) are taken into account by applying radiative corrections:

$$\frac{d^4\sigma}{dQ^2 ds dt d\phi}=F_{\mathrm{rad}}\cdot\int_M^{M+\Delta M}\left[\frac{d^5\sigma}{dQ^2 ds dt d\phi dM_x}\right]_{\mathrm{meas}}dM_x. \tag{2.5}$$

The correction factor F_{rad}, which depends critically on the accepted missing mass interval ΔM, takes into account photon emission, and other second order effects. For details see [9]. The correction factor was applied for each bin of Q^2, s, t, and ϕ and varied between 1.15 and 1.45.

3. Experimental Procedure

3.1. Apparatus

The experimental apparatus is sketched in Fig. 2. The external electron beam from DESY hits a 10 cm long liquid hydrogen or deuterium target. After passing through the target and a secondary emission chamber located 12 m behind the target, the beam is focused onto a Faraday cup which acts as the primary intensity monitor and beam stop.

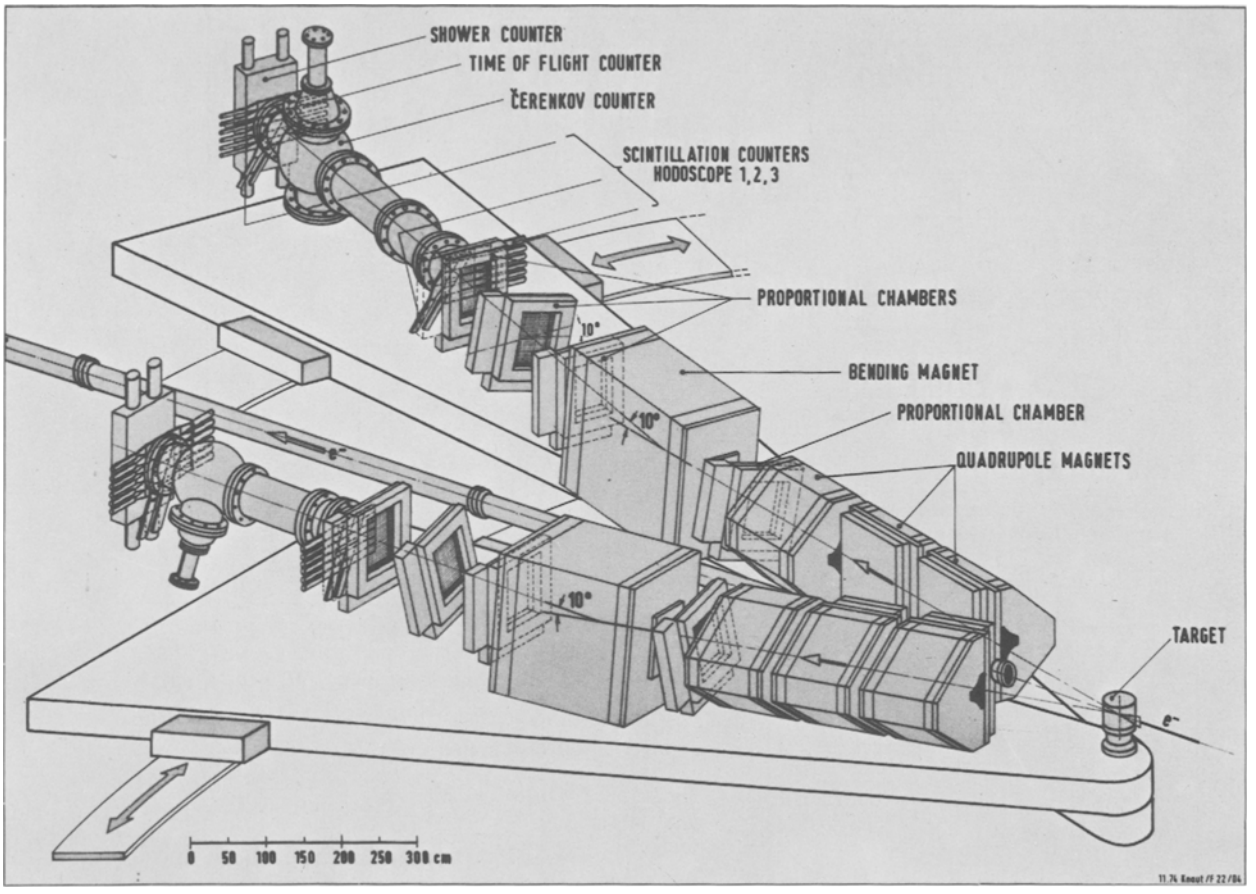

Fig. 2. The experimental setup

Two almost identical magnetic spectrometers detect the scattered electron and the meson in coincidence. Each of the spectrometers consists of three quadrupole magnets followed by a dipole magnet which bends the central trajectory vertically by 10^0. The purpose of the quadrupole magnets was: a) to obtain a large vertical acceptance, which is essential for a measurement of the ϕ-dependence at larger values of $|t|$, b) to remove the scintillation counters and proportional chambers from the high flux of background particles near the target, and c) to maximize the overall acceptance for the given apertures of the bending magnets and the Cerenkov counters. A sketch of the optical system is given in Fig. 3 where the displacement of some special trajectories from the central one is shown. In order to be able to move the spectrometers close to the electron beam, the two quadrupoles near the target were only "half quadrupoles", the second half consisting of an iron mirror plate. The parameters of the spectrometers are listed in Table 1.

A charged particle trajectory was measured with the help of four multiwire proportional chambers, each having two planes of orthogonal read out wires. One chamber was located in front of the bending magnet and three chambers behind it. The momentum of a particle was determined by reconstructing its trajectory through the bending magnet, and the production angles were then obtained by tracing the trajectory through the quadrupole magnets back to the target position. The chambers are followed by two scintillation counter hodoscopes, a threshold Cerenkov counter, two further scintillation counter hodoscopes, and a lead scintillator sandwich shower counter seven radiation lengths thick. The scintillation counter hodoscopes in front of the shower counters were used

Table 1. Parameters (FWHM) of the spectrometer

Momentum resolution $\frac{\Delta p}{p}$ (%)	$(1.1+5.3/p^2)^{1/2}$
Missing mass resolution $\Delta M_X(M_N)$	60 MeV
Acceptance: geometrical	16 mrad horizontal
	200 mrad vertical
momentum	45%

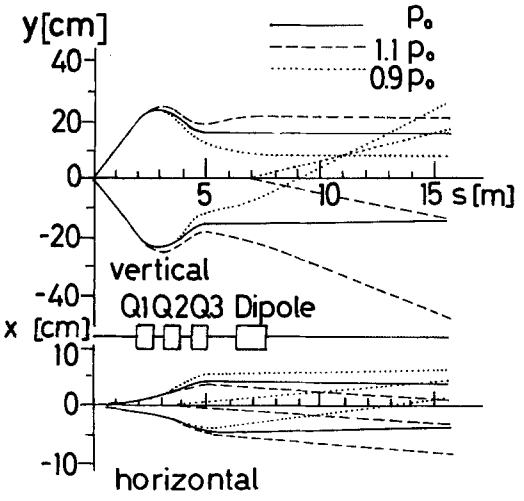

Fig. 3. Trajectories through the magnetic spectrometer for projected angles; $\theta_{vert} = 0, +100, -100$ mrad; $\theta_{hor} = 0, +5, -5$ mrad

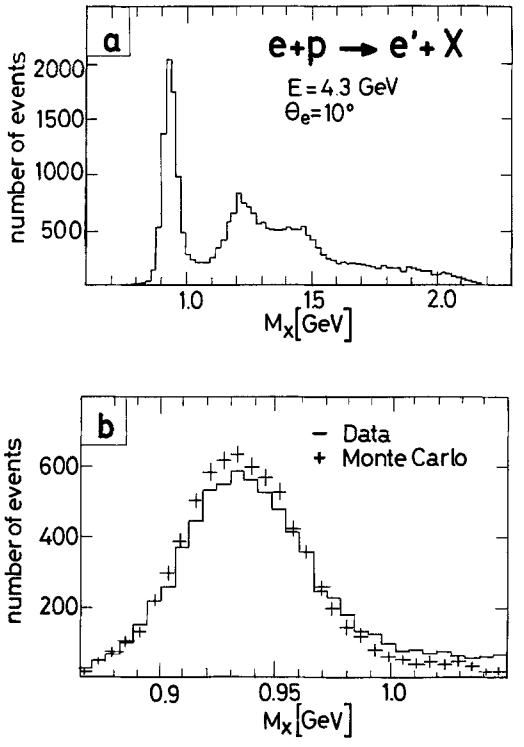

Fig. 4. a Single arm electron missing mass distribution. **b** Comparison of the elastic peak with a Monte Carlo simulation

to measure the time-of-flight difference between electron and hadron. Both Cerenkov counters were filled with ethylene, the one in the electron arm to about atmospheric pressure, and the one in the hadron arm to about 10 atm.

Each spectrometer was mounted on a platform which could be rotated around the target (one arm between 10° and 36°, the other between −9° and −19°).

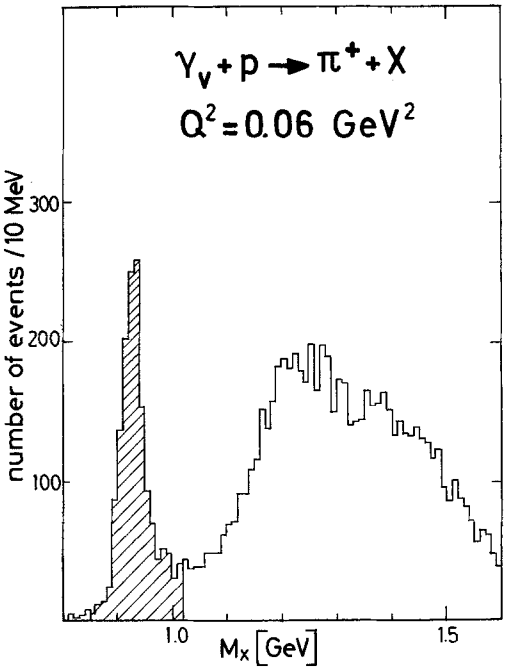

Fig. 5. Missing mass distribution $M_x^2 = (e - e' + p - \pi^+)^2$

3.2. Data Taking

An event was recorded, if in both spectrometers at least three of the four scintillation counter hodoscopes fired within a coincidence time of about 25 nsec. The following information was then transferred to a PDP-8 computer: the hit pattern of the proportional chambers, the gated latches of all counters as well as various counter pulse heights, the pulse overlap width in the various coincidence circuits, the time-of-flight data, and the instantaneous energy of the circulating beam of the synchrotron.

The data of several events were accumulated in the PDP-8 and then transmitted to the central computer. An on-line analysis of clean events was performed and several histograms were generated in order to control the performance of the detector. During each data run various single and coincidence rates were recorded to determine the dead time losses.

3.3. Data Analysis

Apart from small data samples used for efficiency tests, only events were accepted for further analysis which fired the Cerenkov counter in the electron arm. After reconstruction of the trajectory, it was checked whether the trajectory passed through the acceptance defining counters. Rejecting events with a low pulse height in the shower counter eliminates almost all background

in the electron arm, such that it can be even used as a single arm spectrometer as is demonstrated in Fig. 4a where the electron missing mass spectrum, obtained after these cuts, is displayed. In Fig. 4b the elastic peak is drawn separately. Its shape is fairly well reproduced by the results of a Monte Carlo simulation.

The meson detected by the second spectrometer was identified by a threshold Cerenkov counter and by time-of-flight. For the measurements at large values of ε, the pressure of the Cerenkov counter was adjusted to detect pions but no kaons. Separate test runs, performed with a pressure of about 1 atm, showed a negligible background of electron-positron coincidences. The measured pion-momentum was used to calculate the missing mass $M_x^2=(e-e'+p-\pi^+)^2$, a typical distribution of which is shown in Fig. 5. A clear peak is seen at the neutron mass, and events in the hatched region were defined as $(\pi^+ n)$ events.

Kaons were separated from protons by time-of-flight. The flight path from the target to the counters was about 14 m. The start signal was given by the counters in the electron arm. A resolution of 0.8 nsec (FWHM) was achieved. The distribution of particle masses determined from the momentum and velocity measurements is shown in Fig. 6. Rejection of events which triggered the Cerenkov counter eliminated most of the pions. Kaons and protons were well separated. Events within $0.1 \lesssim M_h^2 \lesssim 0.45$ GeV^2 (these limits depended slightly on the hadron momenta) were defined as kaons. The losses due to this cut as well as due to decay in flight were corrected for by a Monte Carlo simulation. The distribution of missing masses $M_x^2=(e-e'+p-K^+)^2$ from these events is shown in Fig. 7.

For the low ε measurements a large electron scattering angle was necessary, and the role of the electron and hadron detecting spectrometers had to be interchanged. The Cerenkov counter in the former electron arm could not be pressurized sufficiently to tag pions and therefore could not be used to separate pions and kaons. However kaons misidentified as pions do not contribute to the $(\pi^+ n)$ data, since these events have missing masses $M_x \geqq 1.18$ GeV. The neutron peak in the M_x spectrum is also clearly identified in these data, as shown in Fig. 8.

3.4. Spectrometer Acceptance

The fourfold differential cross section (2.2), which is a function of the variables $v=(Q^2, s, t, \phi)$ is connected to the event rate $N(\Delta v)$ in a volume element $\Delta v = \Delta Q^2 \cdot \Delta s \cdot \Delta t \cdot \Delta\phi$ via

$$N(\Delta v) = N_e \cdot N_T \cdot \int_{\Delta v} \frac{d\sigma(v)}{dv} a(v) dv. \tag{3.1}$$

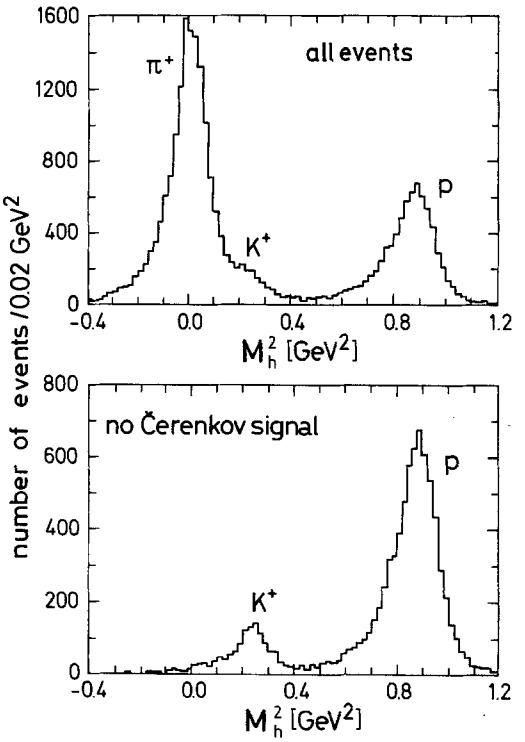

Fig. 6. Hadron mass M_h as calculated from momentum and time-of-flight measurement for $Q^2=1.35$ GeV^2

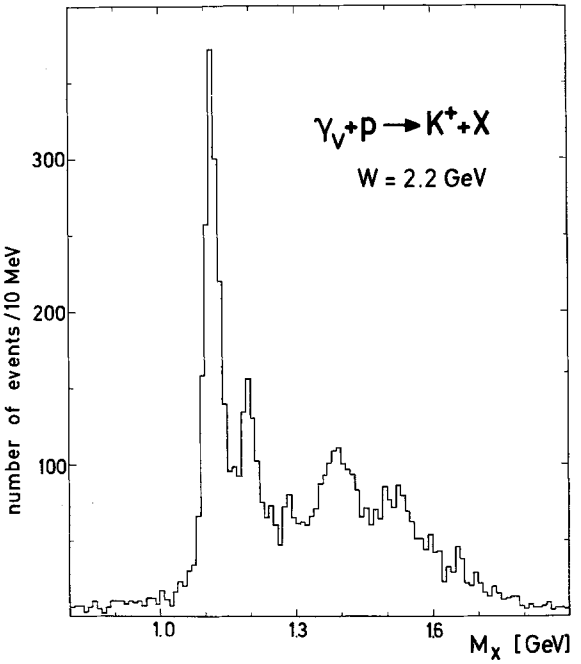

Fig. 7. Missing mass distribution $M_x^2=(e-e'+p-K^+)^2$. The Λ and Σ^0 are clearly visible as well as higher mass hyperons. The structure at 1280 MeV cannot be explained by misidentified pions or protons. Its statistical significance is only about 3σ

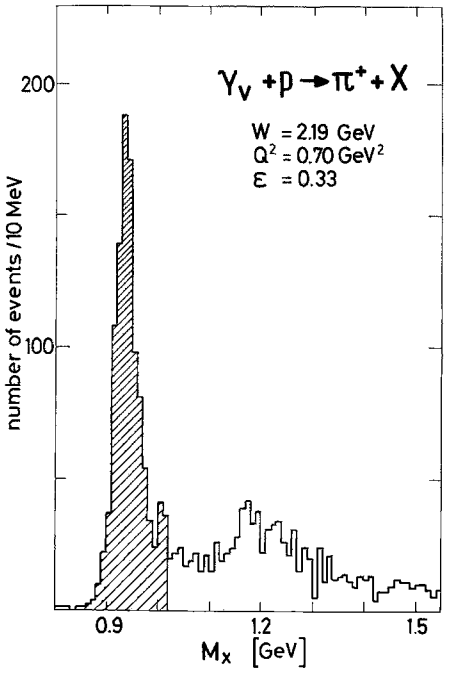

Fig. 8. Missing mass distribution $M_x^2 = (e - e' + p - \pi^+)^2$ for the low ε measurement

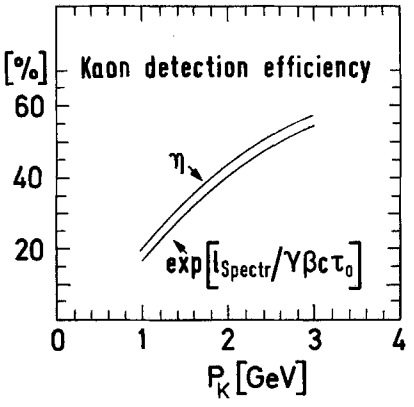

Fig. 9. The kaon detection efficiency η: It is given by the number of K's which did not decay in the spectrometer and the contribution of π^+ and μ^+ from K^+ decay which were identified as kaons. The correction was calculated using Monte Carlo techniques

N_e is the number of incident electrons and N_T the number of target nucleons. The function $a(v)$, which is 1 if both particles are accepted by the spectrometer and 0 otherwise, is determined by Monte Carlo techniques. Inverting (3.1) we obtain

$$\frac{d\sigma(\bar{v})}{dv} = \frac{N(\Delta v)}{N_e \cdot N_T} \cdot \frac{1}{\int_{\Delta v} \frac{g(v)}{g(\bar{v})} a(v) dv} \tag{3.2}$$

where $\bar{v}$ is assumed to be the center of Δv. This assumption is reasonable for the variables t and ϕ since their bin widths are sufficiently small. This is not the case for Q^2 and s, and the acceptance was therefore weighted in (3.2) according to

$$g(Q^2, s) = \Gamma(Q^2, s) \cdot (s - M^2)^{-2} \tag{3.3}$$

which describes roughly the s and Q^2-dependence of the data. (3.2) was used to determine the measured cross sections.

3.5. Corrections

Besides the radiative corrections and the acceptance which we have already mentioned, several other correction factors had to be applied to (3.2) to obtain the cross sections. The biggest one was due to the event reconstruction inefficiency which varied between 16% and 25% per spectrometer and which was continuously monitored. The background from the target walls was at most 10%. The fraction of random coincidences amounted to $\lesssim 4\%$ and the deadtime losses to $\lesssim 3\%$. The absorption corrections were $\lesssim 4\%$.

The losses of pions and kaons due to their decays in flight were determined by detailed Monte Carlo studies. For pions this correction was $\lesssim 3\%$. For kaons this correction was quite significant and as can be seen from Fig. 9 strongly momentum dependent. The time-of-flight measurement was essential for the identification of kaons and at low ε also of pions. It could not be used however, when two or more counters of one hodoscope had fired. This resulted in a correction of about 40% [10, 17].

The overall systematic uncertainty of these corrections together with the uncertainty of the incident electron flux and the target length was estimated to be about 7%. The following tables and plots of our numerical results contain only the statistical errors and not the normalization uncertainty.

4. Results

In this section we present the results. For a comparison with other experiments and with theoretical predictions see Chapt. 5.

4.1. Separation of σ_L, σ_U, σ_P, and σ_I [10]

At $Q^2 = 0.7$ GeV^2 we measured the ϕ and ε dependence of the $(\pi^+ n)$ cross section in order to separate the four terms σ_U, σ_L, σ_P, and σ_I. (When not misleading, we abbreviate the differential terms of 2.4 by σ_U, σ_L, etc.) Data were taken at two different values of the polarization parameter ε. The kinematical parameters of these two measurements are listed in Table 2.

The missing mass distribution for low ε is shown in Fig. 8. Events with $0.85\ \text{GeV} \leqq M_x \leqq 1.02\ \text{GeV}$ were grouped into several (ϕ, t)-bins and weighted with the appropriate acceptance function. The resulting ϕ-distributions are shown in Fig. 10, for two t-bins, together with the best fit based on the ϕ and ε-dependence of 2.4.

The cross sections σ_U, σ_L, σ_P, and σ_I resulting from the fits are listed in Table 3. Only statistical errors were taken into account in this fit. The normalization uncertainties are to a large extent correlated between the two sets of measurements, since the same apparatus and data analysis programs were used, and contribute therefore mainly to the overall normalization of the various cross sections. Making the pessimistic assumption that the normalization of the high and low ε data is different by 6% leaves the cross sections σ_I and σ_P almost unchanged and changes σ_U and σ_L by at most half of the statistical error quoted in Table 3.

The cross sections $\sigma_{\|}$ and $\sigma_{\perp}$, also listed in Table 3, were obtained from a similar fit expressing σ_U and σ_P by $\sigma_{\|}$ and $\sigma_{\perp}$. The quoted errors therefore take the correlation between σ_U and σ_P into account.

4.2. The t and Q^2 Dependence of the $(\pi^+ n)$ Production at Large ε [11]

The π^+ production measurement at large ε covered the following range in Q^2 and t: $0.06 \leqq Q^2 \leqq 1.35\ \text{GeV}^2$; $|t|_{\min} \leqq |t| \leqq 1.2\ \text{GeV}^2$. The cross section $2\pi d^2\sigma/dtd\phi$ is listed in Table 4 as a function of t and ϕ for each Q^2. The accepted ranges of Q^2 and W are given there as well.

The cross sections $\sigma_U + \varepsilon\sigma_L$, σ_P, and σ_I could be separated at smaller values of $|t|$, where the full ϕ-range was covered by the vertical acceptance of the two spectrometer arms. The resulting values are listed in Table 5.

4.3. $(\pi^- p)$ Electroproduction [12]

4.3.1. The experimental method. The reaction

$$\gamma_v + n \to \pi^- + p \tag{4.1}$$

was studied with the help of a deuterium target. The π^- and π^+ missing mass spectra of the processes

$$\gamma_v + d \to \pi^- + p + p_s \tag{4.2}$$

$$\to \pi^+ + n + n_s \tag{4.3}$$

are shown in Fig. 11. The subscript s indicates the spectator nucleon. There are clear peaks at the nucleon mass which are somewhat broader than the π^+ peak in Fig. 5 obtained with a hydrogen target, due to the Fermi motion. Events within $0.85\ \text{GeV} \leqq M_x \leqq 1.02$ GeV were defined as single pion events. A Monte Carlo simulation of the process $\gamma_v + d \to \pi^+ + \Delta^0 + p_s$ indicated a negligible amount of two pion events in this data sample.

The cross section of reaction (4.1) was determined by the ratio method [13]:

$d^4\sigma(\gamma_v + n \to \pi^- + p)$

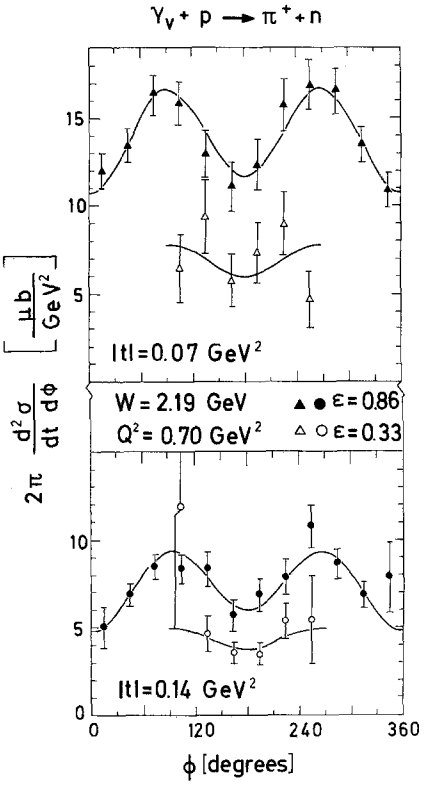

Fig. 10. The ϕ dependence of the $(\pi^+ n)$ cross section $2\pi \frac{d^2\sigma}{dtd\phi}$. The curves show the best $\phi - \varepsilon$-fit to determine the cross section components according to 2.4

Table 2. Kinematical parameters for the σ_L/σ_U separation

	High ε	Low ε
ε	0.86	0.33
W (GeV)	2.06–2.37	2.06–2.37
$\langle W \rangle$ (GeV)	2.19	2.19
Q^2 (GeV^2)	0.55–0.9	0.48–0.9
$\langle Q^2 \rangle$ (GeV^2)	0.70	0.70
E (GeV)	6.0	3.05
E' (GeV)	3.4	0.6
θ_e (deg)	10	36
p_π (GeV)	2.3–1.9	2.35
$\|t\|$ (GeV^2)	$\|t\|_{\min} - 1.2$	$\|t\|_{\min} - 0.28$
ϕ_π (deg)	0–360 ($\|t\| < 0.16$)	90–270 ($\|t\| < 0.16$)
	120–240 ($\|t\| > 0.16$)	120–240 ($\|t\| > 0.16$)

Table 3. Components of the $(\pi^+ n)$ cross section ($Q^2 = 0.70$ GeV^2, $W = 2.19$ GeV)

$\lvert t\rvert$ (GeV^2)	σ_L (μb/GeV^2)	σ_U (μb/GeV^2)	σ_P (μb/GeV^2)	σ_I (μb/GeV^2)	$\sigma_\perp$ (μb/GeV^2)	$\sigma_\parallel$ (μb/GeV^2)	$\phi-\varepsilon$-fit	
							n_D	χ^2/n_D
0.05	15.26±1.97	2.23±1.54	−0.89±0.72	0.06±0.35	3.16±1.72	1.34±1.66	14	1.64
0.07	13.52±1.63	2.29±1.27	−3.16±0.59	−0.26±0.29	5.45±1.40	−0.87±1.36	14	1.03
0.10	8.59±1.39	2.61±1.06	−2.72±0.53	−0.42±0.26	5.33±1.23	−0.11±1.13	14	1.64
0.14	5.93±0.89	2.25±0.65	−2.27±0.46	−0.33±0.22	4.52±0.86	−0.02±0.74	14	0.75
0.18	1.68±0.95	3.78±0.72	−2.47±0.54	−0.02±0.25	6.25±0.92	1.31±0.85	11	1.11
0.24	0.80±1.14	3.76±0.92	−1.87±0.57	0.12±0.27	5.63±1.05	1.89±1.09	10	1.69

Table 4a–d. The $(\pi^+ n)$ cross section $2\pi \frac{d^2\sigma}{dtd\phi}$ (μb/GeV^2) at $W = 2.19$ GeV. The ranges are: W: ≈4.3 − 5.6 GeV; Q^2: 0.035 − 0.09 / 0.22 − 0.34 / 0.55 − 0.9 / 1.2 − 1.5 GeV^2

Table 4a

$Q^2 = 0.06$ GeV^2, $\varepsilon = 0.44$

ϕ (deg)	$\lvert t\rvert$ (GeV^2)							
	0.04	0.12	0.20	0.29	0.42	0.60	0.80	1.05
135	11.83±1.93	10.50±0.78	8.67±0.73	5.23±0.58	2.84±0.40	1.48±0.30	0.72±0.30	
195	10.98±1.73	7.73±0.63	7.99±0.70	5.23±0.59	2.81±0.38	1.90±0.33	1.16±0.27	0.50±0.26

Table 4b

$Q^2 = 0.28$ GeV^2, $\varepsilon = 0.76$

ϕ (deg)	$\lvert t\rvert$ (GeV^2)								
	0.03	0.06	0.12	0.20	0.29	0.42	0.60	0.80	1.05
75	30.41±4.33	24.71±3.06							
105	26.01±2.21	22.93±1.65							
135	21.46±1.89	18.49±1.41							
165	16.32±1.59	15.84±1.37	10.49±0.95	6.24±1.08	4.47±1.22	2.16±0.65	2.33±0.76	1.58±0.74	0.37±0.41
195	18.50±1.79	15.47±1.40	10.16±1.00	6.73±1.14	5.15±1.43	3.69±1.32	1.94±0.73	0.86±0.96	0.45±0.50
225	20.66±2.03	18.46±1.86							
255	30.71±3.08	27.60±2.82							
285	30.14±8.24	22.95±7.38							

Table 4c

$Q^2 = 0.70$ GeV^2, $\varepsilon = 0.86$

ϕ (deg)	$\lvert t\rvert$ (GeV^2)									
	0.05	0.07	0.10	0.14	0.20	0.29	0.42	0.60	0.80	1.05
15	14.83±1.01	12.02±0.97	8.12±0.77	5.09±1.10						
45	15.74±0.99	13.43±0.95	8.23±0.59	6.86±0.62	4.51±0.56	3.44±0.51				
75	16.90±1.04	16.34±1.07	12.14±0.72	8.50±0.66	8.20±0.59	4.45±0.52				
105	15.21±1.12	15.84±1.22	11.92±0.86	8.37±0.80	5.69±0.59	5.59±0.70				
135	14.05±1.19	12.94±1.28	9.29±0.97	8.42±0.96	6.04±0.71	2.91±0.51	2.79±0.42	1.37±0.30	0.81±0.27	0.68±0.27
165	14.67±1.35	11.11±1.37	8.17±0.90	5.70±0.83	3.93±0.61	2.17±0.41	1.94±0.34	0.94±0.22	1.14±0.28	0.11±0.11
195	13.33±1.30	12.32±1.47	9.06±1.00	6.85±0.92	3.41±0.55	2.26±0.43	1.52±0.30	0.99±0.23	0.84±0.24	0.32±0.19
225	17.26±1.39	15.74±1.51	12.66±1.20	7.92±1.03	6.07±0.75	3.73±0.67	3.52±0.57	1.84±0.42	1.15±0.42	0.90±0.35
255	18.53±1.35	16.94±1.42	12.04±1.01	10.79±1.16	6.78±0.88	3.81±0.84				
285	14.03±1.04	16.63±1.20	12.32±0.85	8.67±0.83	7.81±0.77	5.21±0.97				
315	16.21±1.04	13.50±1.02	9.96±0.71	6.87±0.70	6.51±0.70	4.38±0.91				
345	14.74±1.00	10.90±0.95	7.69±0.79	7.86±1.98						

Table 4d

$Q^2 = 1.35$ GeV^2, $\varepsilon = 0.84$

ϕ (deg)	$\lvert t\rvert$ (GeV^2)						
	0.14	0.20	0.29	0.42	0.60	0.80	1.05
15	4.77±0.59	2.86±0.35	2.45±0.38	1.06±0.48			
45	5.91±0.73	3.63±0.43	2.34±0.35	2.12±0.38			
75	4.88±0.69	3.82±0.51	3.62±0.55	1.30±0.40			
105	4.45±0.71	4.17±0.51	2.70±0.46	2.49±0.52			
135	5.12±0.73	3.82±0.63	3.37±0.57	0.83±0.26	1.48±0.33	0.96±0.37	0.36±0.18
165	3.32±0.65	3.13±0.62	1.44±0.35	1.48±0.32	0.62±0.20	0.29±0.14	0.70±0.17
195	3.46±0.67	2.86±0.56	2.04±0.41	1.20±0.29	0.82±0.24	0.98±0.27	0.68±0.16
225	4.57±0.68	2.84±0.54	3.00±0.60	1.25±0.33	1.19±0.34	0.46±0.27	1.00±0.36
255	3.86±0.68	5.37±0.67	2.22±1.12	3.39±0.84			
285	5.30±1.15	5.20±0.70	2.62±0.58	2.54±0.75			
315	5.42±0.78	3.67±0.49	3.52±0.51	1.20±0.33			
345	4.91±0.76	3.96±0.44	2.21±0.36	3.50±1.00			

Table 5. Components of the $(\pi^+ n)$ cross section at high ε ($W = 2.19$ GeV)

$\lvert t\rvert$ (GeV^2)	$\sigma_U + \varepsilon\sigma_L$ (μb/GeV^2)	σ_P (μb/GeV^2)	σ_I (μb/GeV^2)	n_D	$\frac{\chi^2}{n_D}$
$Q^2 = 0.28$ GeV^2	$\varepsilon = 0.76$				
0.03	26.6±4.3	−3.6±4.1	4.4±4.2	5	0.52
0.06	21.5±3.2	−4.1±3.2	2.1±3.1	5	0.56
$Q^2 = 0.70$ GeV^2	$\varepsilon = 0.86$				
0.05	15.34±0.40	−0.97±0.63	0.17±0.32	9	1.45
0.07	13.91±0.35	−3.11±0.54	−0.12±0.28	9	0.41
0.10	9.99±0.29	−2.49±0.46	−0.37±0.23	9	1.36
0.14	7.37±0.25	−1.92±0.43	−0.34±0.22	9	0.70
0.20	5.49±0.35	−2.16±0.63	0.06±0.33	7	2.43
0.29	3.51±0.22	−1.49±0.39	0.11±0.21	7	0.76
$Q^2 = 1.35$ GeV^2	$\varepsilon = 0.84$				
0.14	4.62±0.21	−0.32±0.32	0.41±0.16	9	0.67
0.20	3.68±0.18	−0.83±0.28	0.10±0.13	9	1.29
0.29	2.59±0.16	−0.66±0.26	0.13±0.11	9	1.32
0.42	1.49±0.19	−0.24±0.19	0.11±0.15	9	2.59

$$= \frac{d^4\sigma(\gamma_v + d \to \pi^- + p + p_s)}{d^4\sigma(\gamma_v + d \to \pi^+ + n + n_s)} \cdot d^4\sigma(\gamma_v + p \to \pi^+ + n) \quad (4.4)$$

$$= R \cdot d^4\sigma(\gamma_v + p \to \pi^+ + n).$$

Most of the corrections due to the detailed structure of the deuteron and the final state interactions between the emergent hadrons are expected to cancel out in the ratio R.

A sensitive test of the uncertainties due to these nuclear effects provides a comparison of the π^+ production off hydrogen and deuterium

$$R^+ = \frac{d^4\sigma(\gamma_v + d \to \pi^+ + n + n_s)}{d^4\sigma(\gamma_v + p \to \pi^+ + n)}. \quad (4.5)$$

Corrections for π^+ mesons outside the missing mass cut (indicated by the shaded area in Fig. 11) were determined from a Monte Carlo simulation of the

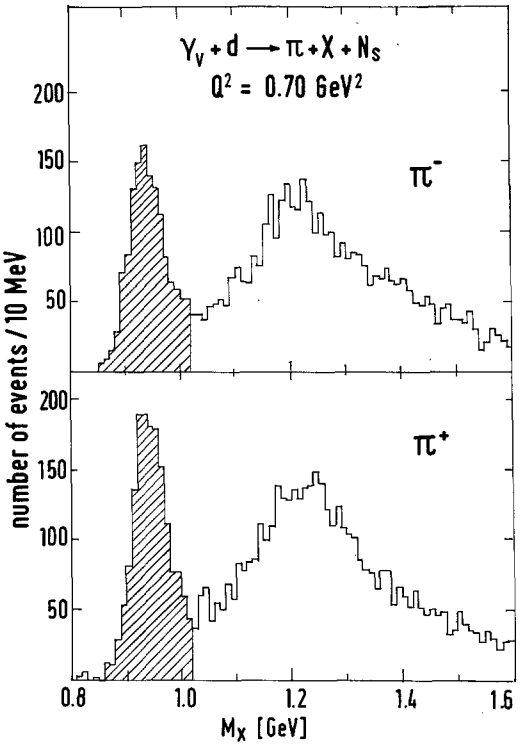

Fig. 11. Spectra of the missing mass $M_x^2 = (e - e' + N - \pi^\pm)^2$ from the deuterium measurement; N indicates the interacting nucleon, N_s the spectator nucleon

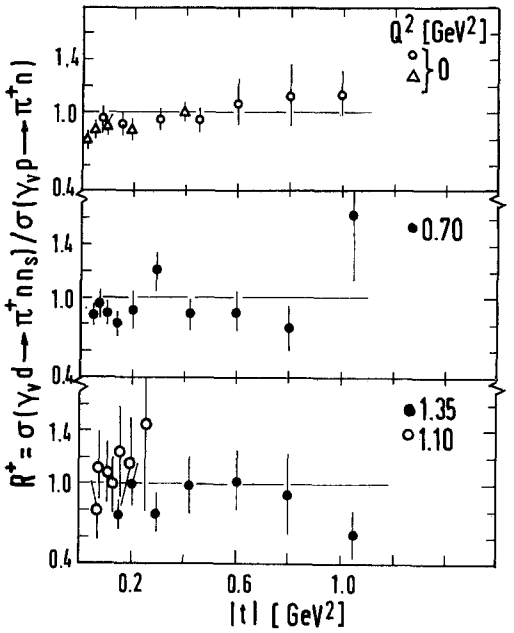

Fig. 12. The ratio of π^+ production off deuterium and off hydrogen. Photoproduction data are from [14, 15, 16]

Table 6. The ratios R and R^+ (see text) and the $(\pi^- p)$ cross section $2\pi \frac{d^2\sigma}{dtd\phi}$ ($W=2.19$ GeV, $120° \leqq \phi \leqq 240°$). The ranges in Q^2/W are: 0.55–0.9 GeV² / 2.1–2.4 GeV and 1.05–1.55 GeV² / 1.8–2.5 GeV

Q^2 (GeV²)	$\lvert t\rvert$ (GeV²)	R^+	R	σ (μb/GeV²)
	0.05	0.87±0.07	0.91±0.08	13.27±1.31
	0.07	0.96±0.10	0.94±0.10	12.12±1.48
	0.10	0.90±0.08	0.94±0.09	8.86±0.99
	0.14	0.81±0.09	0.87±0.10	6.37±0.87
0.70	0.20	0.92±0.10	0.73±0.08	3.49±0.46
	0.29	1.20±0.15	0.51±0.07	1.34±0.23
$\varepsilon=0.86$	0.42	0.89±0.12	0.45±0.07	0.95±0.17
	0.60	0.90±0.14	0.31±0.07	0.38±0.10
	0.80	0.78±0.16	0.22±0.09	0.23±0.11
	1.05	1.633±0.53	0.17±0.10	0.076±0.047
	0.07	—	0.85±0.16	—
	0.10	—	0.83±0.10	—
	0.14	0.77±0.11	0.80±0.11	3.44±0.56
	0.20	1.02±0.16	0.73±0.09	2.24±0.36
1.35	0.29	0.80±0.14	0.55±0.08	1.23±0.23
	0.42	1.00±0.20	0.58±0.10	0.70±0.15
$\varepsilon=0.84$	0.60	1.03±0.23	0.35±0.09	0.32±0.10
	0.80	0.94±0.30	0.34±0.11	0.24±0.09
	1.05	0.62±0.18	0.15±0.10	0.11±0.07

process which took into account the Fermi motion and the bremsstrahlung of the incident and outgoing electron. The ratios R^+ obtained are plotted in Fig. 12, together with similar results from photo- and electroproduction [14–16]. R^+ is found to be slightly smaller than 1, similar to the photoproduction case. Since however most of this small effect is expected to cancel out in the ratio R, we are confident that the cross section (4.4) represents the cross section for π^- production off a free neutron target within the precision obtained in the present experiment.

Table 7. Components of the $(\pi^- p)$ cross section at high ε ($W=2.19$ GeV)

$\lvert t\rvert$ (GeV²)	$\sigma_U+\sigma_L$ (μb/GeV²)	σ_P (μb/GeV²)	σ_I (μb/GeV²)	n_D	$\frac{\chi^2}{n_D}$
$Q^2=0.70$ GeV², $\varepsilon=0.86$					
0.05	12.40±0.61	−0.70±1.01	0.08±0.50	9	1.50
0.07	11.13±0.65	−1.87±1.02	−0.08±0.51	9	0.98
0.10	7.33±0.41	−1.45±0.67	−0.88±0.33	9	1.37
0.14	5.32±0.41	−0.84±0.76	−0.51±0.35	9	0.44
0.20	2.94±0.27	−1.22±0.54	−0.39±0.25	7	1.51
0.29	1.99±0.40	−0.21±0.56	0.39±0.40	7	0.32
$Q^2=1.35$ GeV², $\varepsilon=0.84$					
0.14	3.50±0.28	−0.36±0.44	0.30±0.21	9	0.41
0.20	2.36±0.18	−0.10±0.28	0.18±0.13	9	1.31
0.29	1.63±0.16	−0.18±0.26	0.23±0.11	9	0.39
0.42	0.73±0.12	−0.34±0.21	0.17±0.10	9	0.91

4.3.2. Results on $(\pi^- p)$ production. Measurements were performed at central values of $Q^2=0.70$ GeV² and 1.35 GeV². The ratios R measured within $120° \leqq \phi \leqq 240°$ and the accepted intervals of Q^2 and W are listed in Table 6. Together with the π^+ data from Table 4 we determined the cross section $2\pi \frac{d^2\sigma}{dtd\phi} \cdot (\gamma_v + n \to \pi^- + p)$ which is also listed in Table 6.

Again, at small values of $|t|$ a separation of the different ϕ dependent terms was possible. The results on $\sigma_U+\varepsilon\sigma_L$, σ_I, and σ_P are listed in Table 7.

4.4. $(K^+\Lambda)$ and $(K^+\Sigma^0)$ Production [17]

4.4.1 Data evaluation. The identification of K^+ mesons by time-of-flight and of the recoiling baryons Λ or Σ^0 by missing mass was described in Sect. 3.3. To determine the t and ϕ-dependence of the cross sections, the $\Lambda-\Sigma^0$ separation had to be performed bin by bin. Events in the mass range $1.05 \leqq M_x \leqq 1.15$ GeV were counted as Λ and in the range $1.15 \leqq M_x \leqq 1.25$ GeV as Σ^0. Fitting the Λ and Σ^0 missing mass distribution in the range $M_x \leqq 1.3$ GeV by two Gaussian distributions and a background term yielded results consistent with the above binning.

4.4.2. Results. Data were mainly accepted at ϕ-values around 180°. The cross sections $2\pi d^2\sigma/dtd\phi$ averaged within $120° \leqq \phi \leqq 240°$ are listed in Tables 8 and 9.

Table 8. The $(K^+\Lambda)$ cross section $2\pi \frac{d^2\sigma}{dtd\phi}$ ($120° \leqq \phi \leqq 240°$, $W = 2.21$ GeV). The ranges are: W: $\simeq 1.9-2.5$ GeV, Q^2: 0.02 – 0.11 / 0.20 – 0.37 / 0.55 – 0.85 / 1.0 – 1.6 GeV^2

$Q^2 = 0.06$ GeV^2 $\varepsilon = 0.41$		$Q^2 = 0.28$ GeV^2 $\varepsilon = 0.74$		$Q^2 = 0.70$ GeV^2 $\varepsilon = 0.85$		$Q^2 = 1.35$ GeV^2 $\varepsilon = 0.82$	
$\lvert t\rvert$ (GeV^2)	σ (μb/GeV^2)	$\lvert t\rvert$ (GeV^2)	σ (μb/GeV^2)	$\lvert t\rvert$ (GeV^2)	σ (μb/GeV^2)	$\lvert t\rvert$ (GeV^2)	σ (μb/GeV^2)
		0.09	1.84 ± 0.27				
0.13	1.14 ± 0.29	0.15	1.71 ± 0.24	0.13	1.18 ± 0.15		
0.21	2.44 ± 0.49	0.21	1.25 ± 0.24	0.21	1.49 ± 0.22	0.19	0.87 ± 0.31
0.29	1.71 ± 0.38	0.29	1.47 ± 0.35	0.29	1.06 ± 0.18	0.29	0.42 ± 0.09
0.39	1.04 ± 0.30	0.39	1.25 ± 0.61	0.39	1.13 ± 0.20	0.39	0.28 ± 0.07
0.52	1.20 ± 0.36	0.52	0.75 ± 0.43	0.52	0.64 ± 0.13	0.52	0.28 ± 0.07
0.75	0.79 ± 0.23			0.75	0.28 ± 0.08	0.75	0.26 ± 0.05
1.05	0.46 ± 0.27			1.05	0.30 ± 0.10	1.05	0.17 ± 0.05
						1.44	0.15 ± 0.05

Table 9. The $(K^+\Sigma^0)$ cross section $2\pi \frac{d^2\sigma}{dtd\phi}$ ($120° \leqq \phi \leqq 240°$, $W = 2.21$ GeV). The ranges in W and Q^2 are the same as in Table 8

$Q^2 = 0.06$ GeV^2 $\varepsilon = 0.41$		$Q^2 = 0.28$ GeV^2 $\varepsilon = 0.74$		$Q^2 = 0.70$ GeV^2 $\varepsilon = 0.85$		$Q^2 = 1.35$ GeV^2 $\varepsilon = 0.82$	
$\lvert t\rvert$ (GeV^2)	σ (μb/GeV^2)	$\lvert t\rvert$ (GeV^2)	σ (μb/GeV^2)	$\lvert t\rvert$ (GeV^2)	σ (μb/GeV^2)	$\lvert t\rvert$ (GeV^2)	σ (μb/GeV^2)
		0.09	0.76 ± 0.20				
0.13	1.56 ± 0.40	0.15	1.14 ± 0.19	0.15	0.24 ± 0.10		
0.21	1.32 ± 0.32	0.21	1.11 ± 0.23	0.21	0.28 ± 0.08		
0.29	1.17 ± 0.31	0.29	0.87 ± 0.21	0.29	0.26 ± 0.07	0.29	0.15 ± 0.07
0.39	1.10 ± 0.37	0.39	0.61 ± 0.33	0.39	0.35 ± 0.10	0.39	0.15 ± 0.04
0.52	0.87 ± 0.30	0.52	0.99 ± 0.45	0.52	0.27 ± 0.08	0.52	0.10 ± 0.04
0.75	0.98 ± 0.26			0.75	0.24 ± 0.07	0.75	0.08 ± 0.03
1.05	0.88 ± 0.42			1.05	0.18 ± 0.08	1.05	0.14 ± 0.05
						1.44	0.06 ± 0.03

Table 10. Components of the $(K^+\Lambda)$ cross section at high ε ($W = 2.21$ (GeV)

$\lvert t\rvert$ (GeV^2)	$\sigma_U + \varepsilon\sigma_L$ (μb/GeV^2)	σ_P (μb/GeV^2)	σ_I (μb/GeV^2)	n_D	$\frac{\chi^2}{n_D}$
$Q^2 = 0.70$ GeV^2, $\varepsilon = 0.85$					
0.13	1.34 ± 0.11	-0.03 ± 0.20	0.15 ± 0.09	3	1.27
0.21	1.34 ± 0.10	0.17 ± 0.19	0.01 ± 0.09	3	0.97
0.29	0.87 ± 0.09	0.19 ± 0.16	0.04 ± 0.08	3	0.50
$Q^2 = 1.35$ GeV^2, $\varepsilon = 0.82$					
0.19	0.94 ± 0.16	0.02 ± 0.31	0.05 ± 0.14	3	0.50
0.29	0.37 ± 0.06	0.05 ± 0.13	0.03 ± 0.05	3	1.50
0.39	0.23 ± 0.05	-0.09 ± 0.11	-0.02 ± 0.04	3	2.03
0.52	0.23 ± 0.05	-0.10 ± 0.11	0.00 ± 0.04	3	1.60

Table 11. Components of the $(K^+\Sigma^0)$ cross section at high ε ($W = 2.21$ (GeV)

$\lvert t\rvert$ (GeV^2)	$\sigma_U + \varepsilon\sigma_L$ (μb/GeV^2)	σ_P (μb/GeV^2)	σ_I (μb/GeV^2)	n_D	$\frac{\chi^2}{n_D}$
$Q^2 = 0.70$ GeV^2, $\varepsilon = 0.85$					
0.15	0.34 ± 0.09	0.03 ± 0.16	0.08 ± 0.09	3	0.07
0.21	0.30 ± 0.04	-0.12 ± 0.09	0.00 ± 0.04	3	0.50
0.29	0.42 ± 0.05	-0.20 ± 0.10	0.08 ± 0.04	3	1.03
$Q^2 = 1.35$ GeV^2, $\varepsilon = 0.82$					
0.29	0.16 ± 0.04	-0.08 ± 0.09	0.01 ± 0.03	3	0.50
0.39	0.13 ± 0.04	-0.10 ± 0.09	0.00 ± 0.03	3	2.10
0.52	0.12 ± 0.03	-0.13 ± 0.07	-0.01 ± 0.02	3	0.03

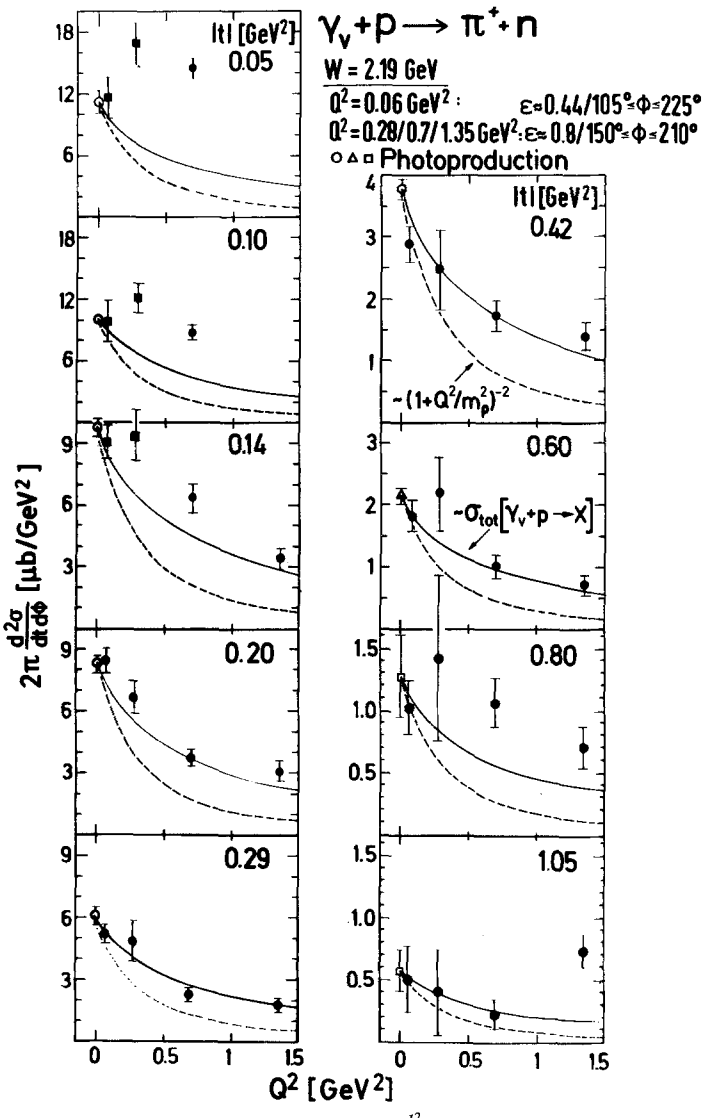

Fig. 13. The $(\pi^+ n)$ cross section $2\pi \frac{d^2\sigma}{dtd\phi}$ versus Q^2. Photoproduction data are from [18, 19]

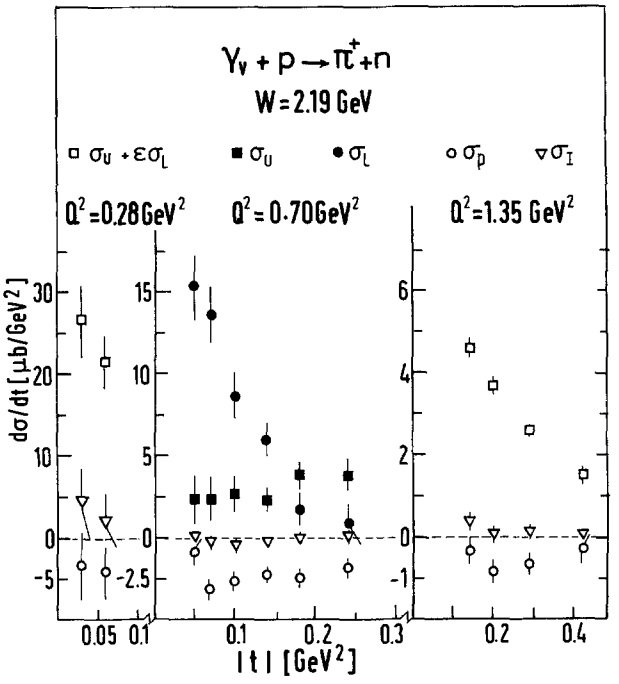

Fig. 14. Components of the $(\pi^+ n)$ cross section corresponding to different spin states of the virtual photon

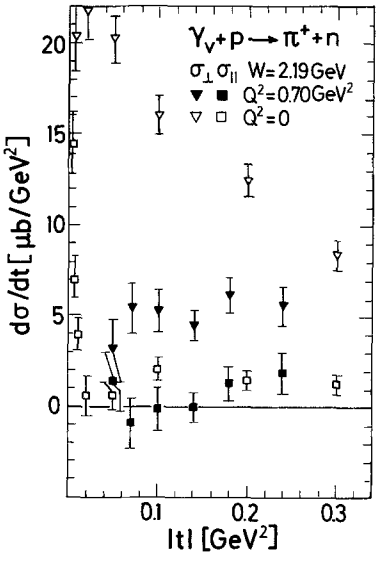

Fig. 15. The $(\pi^+ n)$ transverse cross sections $d\sigma_\perp/dt$ and $d\sigma_{||}/dt$ compared with photoproduction data from [14, 20]

The ϕ-acceptance was at $Q^2 = 0.70$ and 1.35 GeV^2 and small $|t|$ sufficiently large to separate $\sigma_U + \varepsilon\sigma_L$, σ_I, and σ_P. The results are listed in Tables 10 and 11.

5. Discussion

We start with the charged pion production at low $|t|$ and extend the discussion in 5.2 to the more complex case of larger $|t|$. For a discussion of the π^- data we refer to Sect. 5.3 and for the $(K^+\Lambda)$ and $(K^+\Sigma^0)$ data to Sect. 5.4.

5.1. Forward Pion Production

The $(\pi^+ n)$ cross section $2\pi d^2\sigma/dtd\phi$ covering the full Q^2 and t range of this experiment is shown in Fig. 13 as a function of Q^2 for various t values. The $Q^2 = 0.06$ GeV^2 data show reasonable agreement with the photoproduction results [18, 19]. For $|t| = 0.05$ GeV^2 however, the cross section at $Q^2 = 0.28$ and 0.70 GeV^2 significantly exceeds the photoproduction value. (At $Q^2 = 1.35$ GeV^2 the minimum momentum transfer $|t|_{min}$ is already 0.1 GeV^2). This increase in cross section is due to the dominance of $\sigma_U + \varepsilon\sigma_L$ at small $|t|$ as is

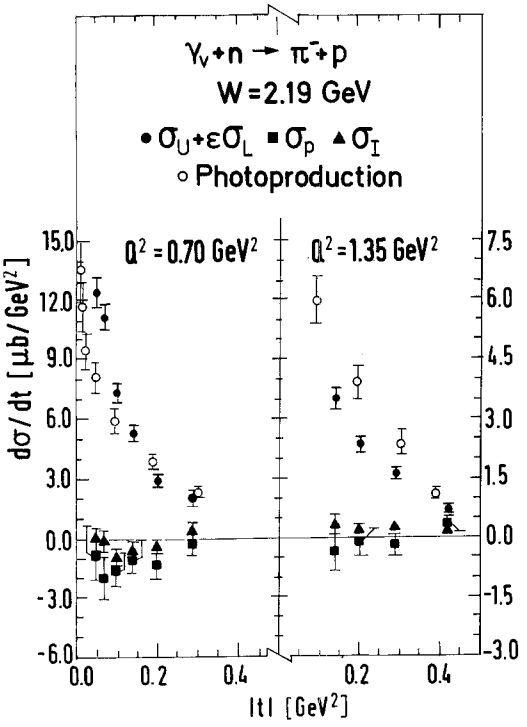

Fig. 16. Components of the $(\pi^- p)$ cross sections corresponding to different spin states of the virtual photon. The photoproduction data (σ_U) are from [14]

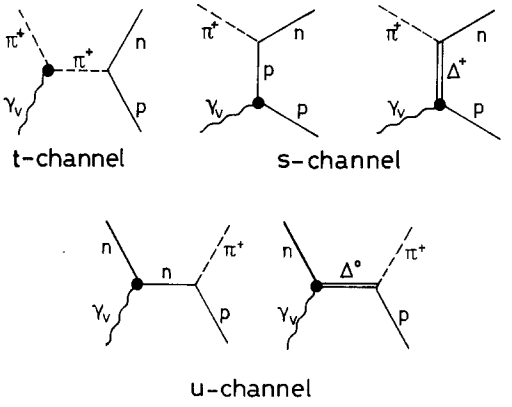

Fig. 17. Born term model diagrams for the reaction $\gamma_v + p \to \pi^+ + n$

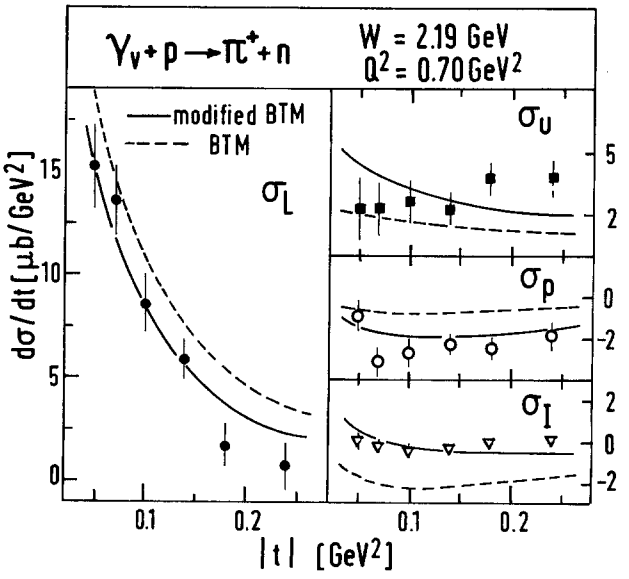

Fig. 18. The four $(\pi^+ n)$ cross section components compared with predictions from the Born term model and its modified version according to [6]

evident from Fig. 14, where the terms of different ϕ-dependence $\sigma_U + \varepsilon\sigma_L$, σ_P, and σ_I are plotted. The data from our measurements at high and low ε at $Q^2 = 0.70$ GeV^2 show that $\sigma_L \gg \sigma_U$ for $|t| < 0.1$ GeV^2. Since $\sigma_L = 0$ at $Q^2 = 0$, this provides a natural explanation for the increase of the cross section with Q^2 at low $|t|$. The transverse cross section components $\sigma_{\|}$ and $\sigma_\perp$, obtained from the data at $Q^2 = 0.70$ GeV^2, are compared with the corresponding photoproduction results [14, 20] in Fig. 15. As in photoproduction $\sigma_\perp > \sigma_{\|}$ within the range of our data. But $\sigma_\perp$ is only about 1/4 of the photoproduction value at low $|t|$.

The π^- data measured at $Q^2 = 0.70$ and 1.35 GeV^2 show some similarity with the π^+ data at low $|t|$. In Fig. 16 the ϕ-dependent terms are compared with photoproduction results [14]. The cross section $\sigma_U + \varepsilon\sigma_L$ is again dominating and for $|t| \lesssim 0.1$ GeV^2 exceeds the photoproduction result by up to 50% at $Q^2 = 0.70$ GeV^2.

5.1.1 Comparison with the Born term model. Charged pion photo- and electroproduction data at low $|t|$-values have been reasonably described by the Born term model (BTM), which is based on the diagrams shown in Fig. 17. The longitudinal cross section σ_L is, within the framework of the BTM, at low $|t|$ dominated by the one pion exchange diagram. Single pion electroproduction data have therefore been used to determine F_π. Experiments, however, which did not separate σ_U and σ_L required a model dependent calculation of σ_U. Following [6] and using on shell nucleon form factors

$$G_E^p(Q^2) = G_M^p(Q^2)/\mu_p = G_M^n(Q^2)/\mu_n = \left(1 + \frac{Q^2}{0.71}\right)^{-2},$$

$$G_E^n(Q^2) = 0$$

and $F_\pi(Q^2) = (1 + Q^2/m_\varrho^2)^{-1}$ we obtain the dashed line displayed in Fig. 18. These results roughly reproduce σ_U and σ_L but fail to describe σ_I and σ_P.

It was noticed by Gutbrod and Kramer [6] that modifying the BTM by treating $G_E^p(Q^2)$ as a free parameter (perhaps justified by the fact that the nucleon is far off its mass shell whereas the pion is near to its pole) improves the agreement with the data

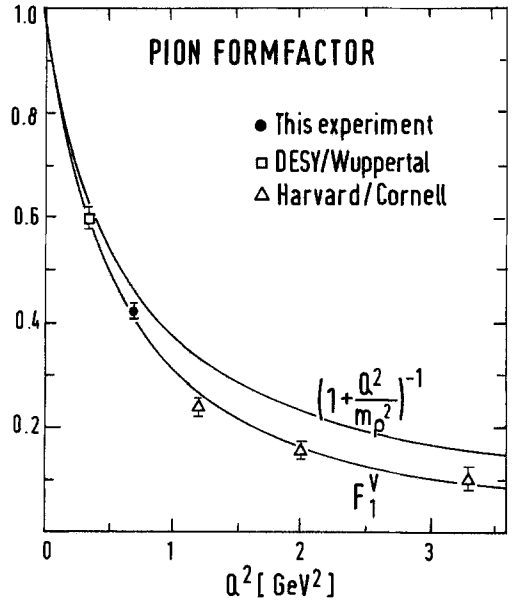

Fig. 19. The electromagnetic pion formfactor as determined in experiments which separated the transverse and the longitudinal $(\pi^+ n)$ cross section. The curve F_1^v is calculated using the parametrisation of the nucleon form factors described in Sect. 5.1.1

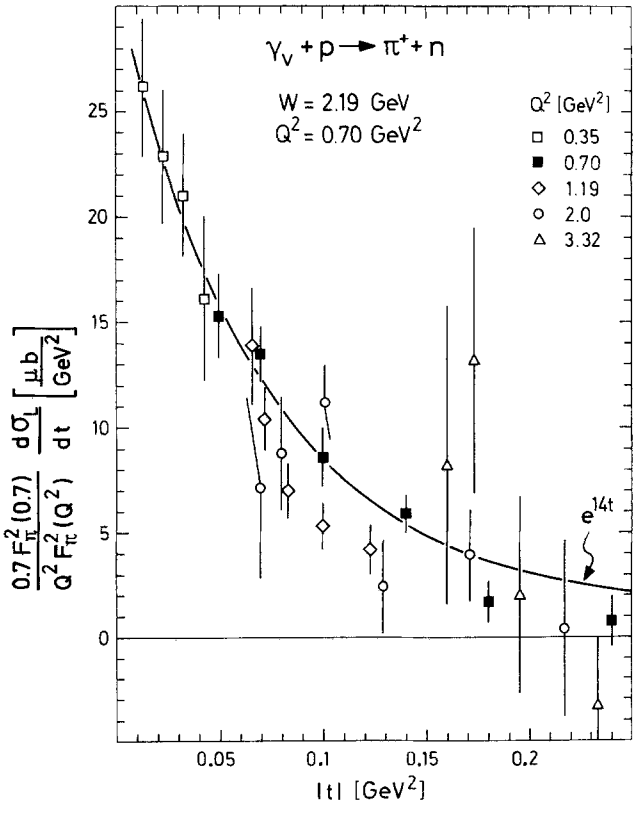

Fig. 20. The $(\pi^+ n)$ longitudinal cross section. The data from other experiments [21, 23] are scaled in W and Q^2

significantly. The results of a fit with F_π and G_E^p as free parameters are shown as solid line in Fig. 18. The best fit yields $F_\pi(Q^2=0.70\,\text{GeV}^2)=0.42\pm0.015$ and nucleon form factors about 50% above their on mass shell values. Recent results for F_π obtained by similar techniques are plotted in Fig. 19. Only data [21, 22] based on a separate determination of σ_U and σ_L are included in this plot. In this Q^2 region the data on F_π of the different experiments are consistently below the ρ-pole prediction. The Q^2-dependence resembles closely the one of the isovector Dirac form factor of the nucleon F_1^V.

Apart from an improved description of σ_U and σ_L, the modified BTM [6] predicts a slower decrease of σ_U with increasing Q^2 which is in full agreement with our data. The experimental uncertainties on σ_U are however still quite large and we postpone a discussion on the Q^2-dependence of σ_U to the next section.

5.1.2. The Q^2 and t-dependence of σ_L and σ_U. Two other experimental groups [21, 23] have recently separated σ_U and σ_L in π^+ electroproduction above the resonance region. In order to compare results, we scaled their cross sections according to $(W^2-M^2)^{-2}$. This W-dependence provides a good parametrisation of the photo- and electroproduction data at small $|t|$ [11, 24, 25]. Figure 20 summarizes the results on σ_L which lie on a universal curve when scaled with $Q^2 \cdot F_\pi^2(Q^2)$. This is not surprising, since at high s $Q^2 \cdot F_\pi^2(Q^2)$ presents the leading Q^2-dependence in the BTM which was used to determine F_π. The Harvard-Cornell data [23] at $Q^2=1.19$ GeV^2 are below this curve, but this might be caused by some slight normalization error, since the corresponding σ_U results are significantly higher than other data nearby in Q^2. The longitudinal cross section σ_L decreases rapidly with increasing $|t|$. Fitting our data with an exponential $e^{-b|t|}$, we obtain with $b=(14\pm2)$ GeV^{-2} a slope parameter which also describes the other data in Fig. 20 well. Assuming that the pion pole contribution and the residual t-dependence $e^{-B|t|}$ factorize, we get from our data $B=(5.6\pm2)$ GeV^{-2}.

The different data on σ_U are compiled in Fig. 21. No scaling in Q^2 was applied. The cross section, especially at small $|t|$, drops steeply from $Q^2=0$ to $Q^2=0.35$ GeV^2. No significant Q^2 or t-dependence is however observable between $Q^2=0.35$ and 3.32 GeV^2. Figure 22 shows the Q^2-dependence of σ_U at $|t|\simeq0.05$ GeV^2. The data above $Q^2=1$ GeV^2 are from somewhat larger $|t|$ [23]. Estimates of σ_U obtained from our large ε data at $Q^2=0.06$, 0.28, and 1.35 GeV^2 are also included in Fig. 22. They are based on the $\sigma_U+\varepsilon\sigma_L$ data from Table 5 and on interpolations of σ_L from Fig. 20. For the $Q^2=0.06$ GeV^2 estimate, we assume σ_P and σ_I to be negligible and use the data on $2\pi d^2\sigma/$

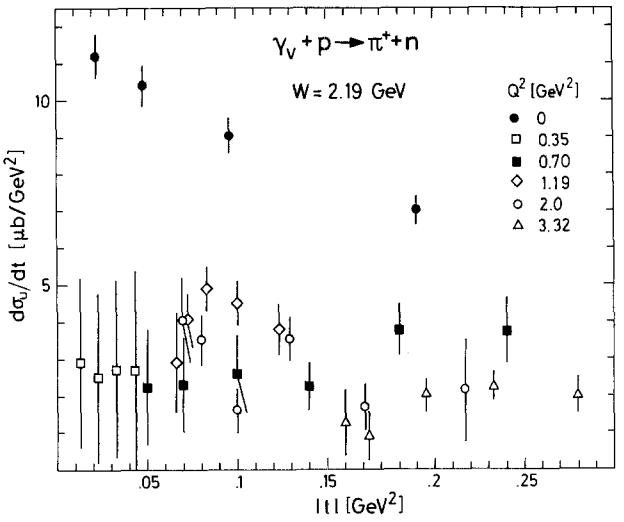

Fig. 21. The $(\pi^+ n)$ transverse cross section. The data from other experiments [14, 21, 23] are scaled in W

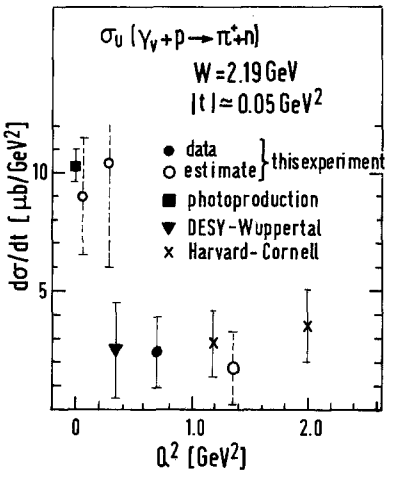

Fig. 22. The Q^2 dependence of the transverse $(\pi^+ n)$ cross section at $|t| \simeq 0.05$ GeV^2. The data from other experiments [14, 21, 23] are scaled in W

$dtd\phi$ from Table 4a. There is some disagreement between our estimate at $Q^2 = 0.28$ GeV^2 and the value at $Q^2 = 0.35$ GeV^2 obtained by the DESY-Wuppertal group [21]. Nevertheless, Fig. 22 shows that σ_U is roughly independent of Q^2 for $Q^2 \gtrsim 0.5$ GeV^2. The decrease of the cross section at small Q^2 seems to become less significant as $|t|$ increases.

5.2. $(\pi^+ n)$ Production at Larger $|t|$

At larger $|t|$ only a limited ϕ-interval around 180° was accepted by the apparatus which did not allow for a separation of cross sections. We therefore plot in Fig. 23 the cross section $2\pi d^2\sigma/dtd\phi$, averaged within the indicated ϕ-intervals.

The data in Fig. 23 show little Q^2-dependence for $|t| \geqq 0.80$ GeV^2. This is consistent with the findings at low $|t|$ of Sect. 5.1: σ_L is steeply decreasing with $|t|$; its contribution at $|t| \simeq 0.8$ GeV^2 is expected to be negligible, and the Q^2-dependence of σ_U diminishes with increasing $|t|$. This trend becomes even clearer if we compare our data with the data from the Harvard-Cornell group [16, 27]. This is done in Fig. 24. The low $|t|$ data of [16] were converted from $d\sigma/d\Omega$ to $d\sigma/dt$ and scaled to the nominal value of W according to $(W^2 - M^2)^{-2}$. The data at $|t| \geqq 1$ GeV^2 of [27] were extrapolated to the nominal W according to the functional dependence given there and then converted to $d\sigma/dt$. Figure 24 shows cross sections which are roughly independent of Q^2 for $|t| \gtrsim 0.2$ GeV^2 and $Q^2 \geqq 0.7$ GeV^2. The t-dependence is roughly $e^{-8|t|}$ at low $|t|$ and $e^{-1.2|t|}$ for $|t| > 1$ GeV^2. For $|t| \gtrsim 1$ GeV^2 the data show no Q^2-dependence at all within the experimental

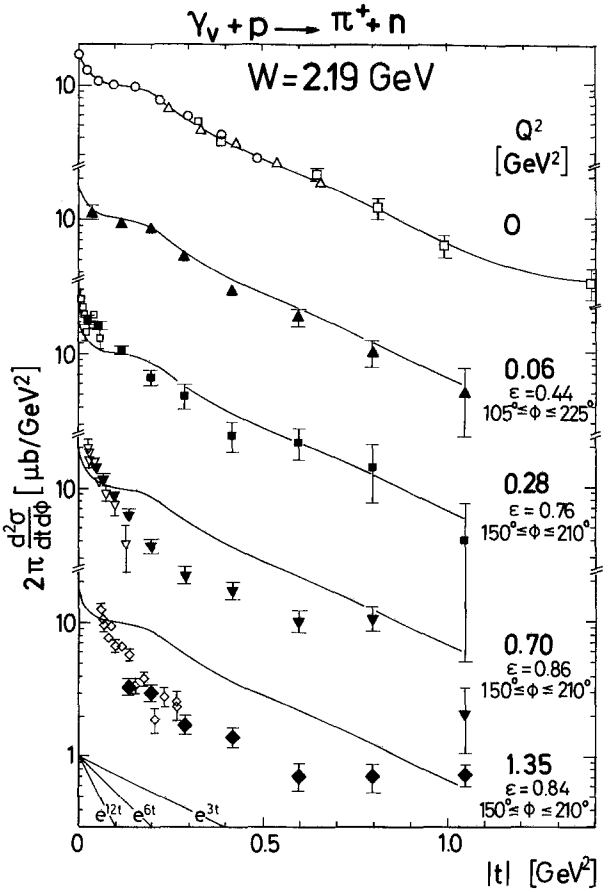

Fig. 23. The $(\pi^+ n)$ cross section $2\pi d^2\sigma/dtd\phi$. The photoproduction data are from [18, 19]. The other open symbols show data from the Harvard/Cornell group [5, 26] at (Q^2 (GeV^2), ε, φ)≈(0.26, 0.9, 150°–180°), (0.70, 0.75, 150°–180°), (1.1, 0.9, 135°–225°). These data are scaled in W

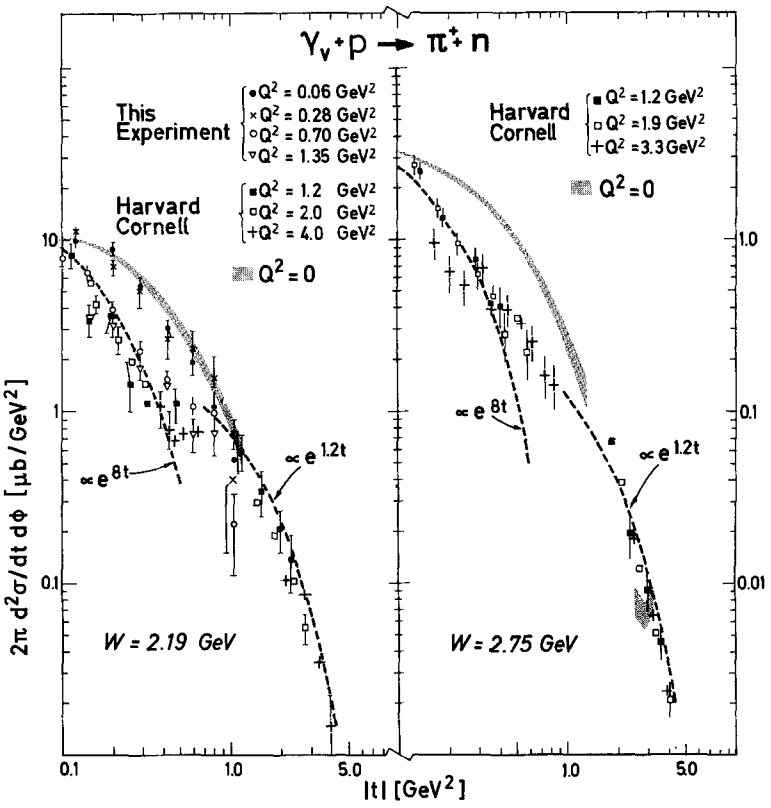

Fig. 24. The $(\pi^+ n)$ cross section $2\pi d^2\sigma/dtd\phi$. The data from Fig. 23 are shown with data from [16] ($|t|<1$ GeV^2; $\varepsilon \simeq 0.9$; $135° < \phi < 225°$ for low W and $-45° < \phi < 45°$ for high W) and from [27] ($|t|>1$ GeV^2, $\varepsilon \simeq 0.9$, $100° < \phi < 150°$). These data are scaled in W as described in the text. The photoproduction data at $|t| \simeq 3$ GeV^2 are from [28] (see text)

Table 12. Integrated $(\pi^+ n)$ and total cross section and their ratio (see text). σ_{tot} is taken from [29, 30]

Q^2 (GeV^2)	ω'	$\sigma(\pi^+ n)$ (μb)	σ_{tot} (μb)	$R_{tot}^{\pi^+ n}$ (%)	Ref.
$W=2.19$ GeV					
0		4.8±0.1	148 ±7	3.2±0.17	[18, 19]
0.06	81	4.4±0.3	131 ±7	3.4±0.3	This exp.
0.28	18	4.8±0.5	95.7±4	5.0±0.6	This exp.
0.70	7.9	3.1±0.2	64.3±2.2	4.8±0.35	This exp.
1.17	5.1	2.2±0.5	46.1±1.5	4.8±1.1	[16, 27]
1.35	4.6	1.9±0.2	41.1±1.4	4.6±0.5	This exp.
1.86	3.6	1.5±0.4	30.6±1.0	4.9±1.3	[16, 27]
3.75	2.3	0.6±0.1	12.1±0.5	5.0±0.9	[16, 27]
$W=2.75$ GeV					
0		1.5±0.1	127±7	1.2±0.1	[14, 19]
1.2	7.3	1.0±0.2	38.9±0.9	2.6±0.5	[16, 27]
1.9	5.0	0.74±0.15	27.4±0.6	2.7±0.5	[16, 27]
3.48	3.2	0.39±0.1	14.8±0.3	2.6±0.7	[16, 27]

uncertainties. We plot in Fig. 24 the Harvard-Cornell data [16] around $W=2.75$ GeV as well (here the $|t| \leqq 0.9$ GeV^2 data were taken in the interval $-45° \leqq \phi \leqq 45°$). They show qualitatively the same behaviour. The photoproduction data [28] show at $|t| \simeq 3$ GeV^2 were taken at $\theta_{\gamma\pi}^{CMS} \approx 90°$ and scaled from $W=2.9$ GeV according to the W-dependence of [28].

5.2.1. The integrated $(\pi^+ n)$ cross section and correspondence arguments. To obtain an estimate of the total $(\pi^+ n)$ cross section $\sigma(\pi^+ n)$, we integrate the data in Fig. 24 over t for each Q^2. We use the measured data at $|t| \leqq 1.2$ GeV^2 and extrapolate according to $e^{-1.2|t|}$ as indicated in Fig. 24. This extrapolation amounts to at most 20% of the integral but of course takes no possible backward peak into account. For $Q^2 > 0.7$ GeV^2 the Q^2-dependence of $\sigma(\pi^+ n)$ is mainly determined by the variation of $|t|_{min}$.

The results of this integration are compiled in Table 12. Figure 25 shows these results normalized to the total cross sections, obtained from [29, 30]. The ratio rises significantly from photoproduction to $Q^2 = 0.28$ GeV^2 and remains then constant up to $Q^2 = 4$ GeV^2. An explanation for this relative increase compared to photoproduction is provided by the longitudinal cross section. It seems however unlikely that σ_L significantly contributes even at $Q^2 = 4.0$ GeV^2 in view of the strong t-dependence of σ_L and the fact that $|t|_{min}(Q^2 = 4$ GeV^2, $W = 2.19$ GeV$) = 0.4$ GeV^2.

The ratio of nondiffractive exclusive electroproduction to total electroproduction cross section was predicted by Bjorken and Kogut [31] to be roughly independent of Q^2 at fixed W. This prediction is based on so called "correspondence arguments", where one assumes the continuity of dynamics between an unknown kinematical region and a neighbouring

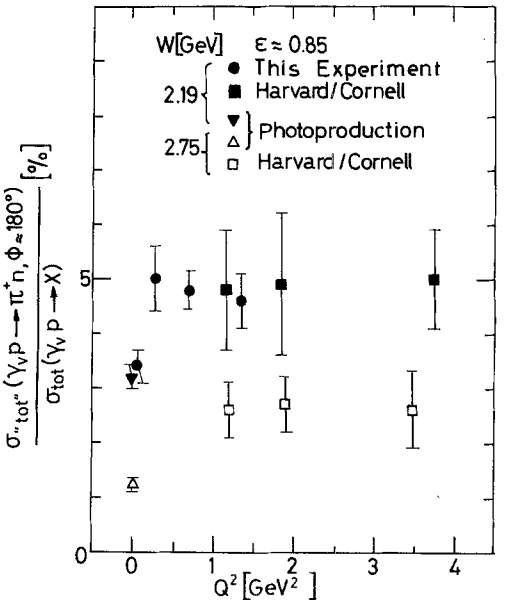

Fig. 25. The integrated ($\pi^+ n$) cross section, normalized to the total photo- resp. electroproduction cross section

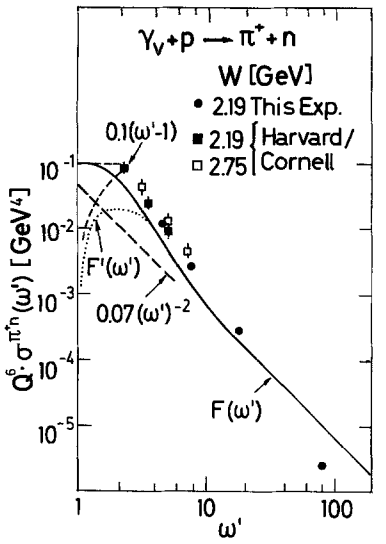

Fig. 26. The prediction of the "correspondence hypothesis" [31], compared to the data of Fig. 25. $F(\omega')$ and $F'(\omega')$ apply only to the transverse part of $\sigma(\pi^+ n)$

known one. For the $\gamma_v + p \to \pi^+ + n$ process the authors conclude that the product $Q^6 \cdot \sigma(\pi^+ n)$ should roughly scale:

$$Q^6 \cdot \sigma(\pi^+ n) = F(\omega'), \qquad \omega' = \frac{W^2}{Q^2} + 1. \tag{5.1}$$

A semiquantitative estimate yields for the transverse part of $\sigma(\pi^+ n)$

$$F(\omega') \approx 0.07\,(\omega' - 1)^{-2}, \qquad \omega' \gtrsim 4 \tag{5.2}$$

$$F(\omega') \approx 0.1, \qquad \omega' \approx 1. \tag{5.3}$$

Instead of (5.3) Bjorken and Kogut obtain

$$F'(\omega') \approx 0.1\,(\omega' - 1), \qquad \omega' \approx 1. \tag{5.3'}$$

Equation (5.3) [11] is based on consistent use of the different conventions [32, 33] relating the structure function νW_2 with σ_{tot}. It describes the data better and seems to be equally well justified within the uncertainties of the arguments.

The curve $F(\omega')$ shown in Fig. 26, which for $\omega' \gtrsim 4$ is taken from [31], interpolates between the two regions in ω'. The data of Table 12 are shown in Fig. 26 as well. They follow surprisingly close these rough theoretical estimates.

5.3. The π^-/π^+ Ratio and $(\pi^- p)$ Production

The π^-/π^+ cross section ratio R was measured at $Q^2 = 0.70$ and 1.35 GeV^2. R is shown in Fig. 27 as a

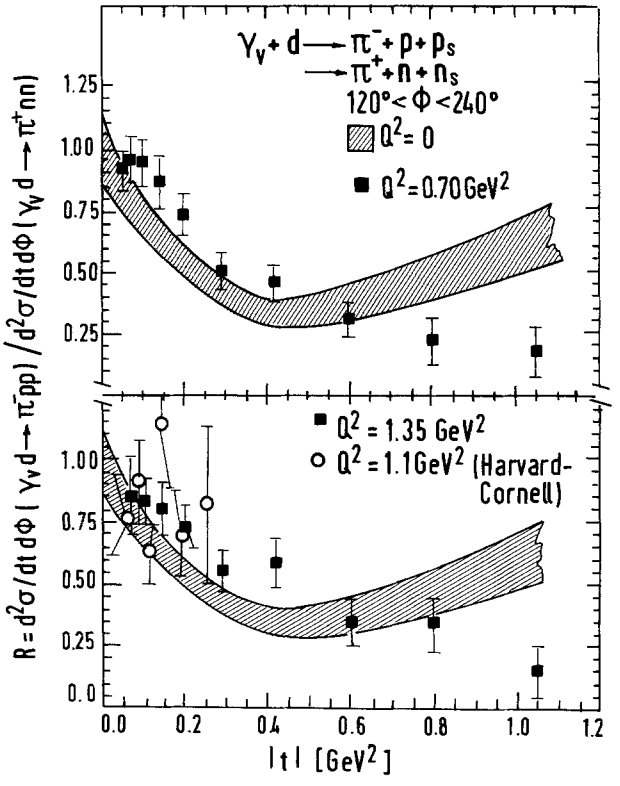

Fig. 27. The ratio of π^- to π^+ production off deuterium. Data at $Q^2 = 0$ are from [14, 15], those at $Q^2 = 1.1$ GeV^2 ($135° < \phi < 225°$) are from [16]

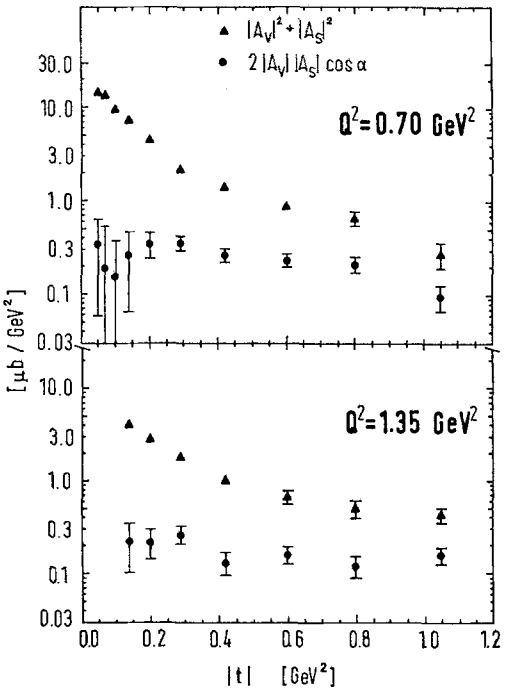

Fig. 28. Sum and interference term of the isovector and isoscalar amplitudes for pion electroproduction at $W=2.19$ GeV

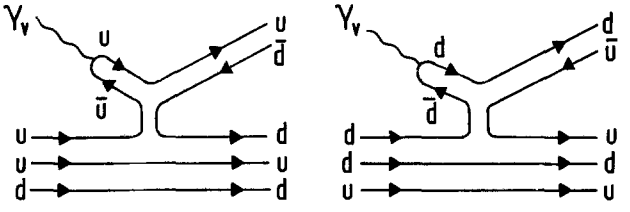

Fig. 29. s-channel quark line diagrams for the reactions $\gamma_v+p\to\pi^++n$ and $\gamma_v+n\to\pi^-+p$

function of $|t|$. The photoproduction results [14, 15] as well as data from the Harvard-Cornell group [16] are also indicated. The electroproduction data differ in two respects from photoproduction: At small $|t|$ the ratio R drops slower with increasing $|t|$ than in photoproduction. This effect is probably due to σ_L which is expected to contribute equally to the π^- and π^+ channel. This explanation is strongly supported by the data in Fig. 16 which show that at low $|t|\sigma_U+\varepsilon\sigma_L$ is the dominating contribution also in the $(\pi^- p)$ channel, and that at $Q^2=0.70$ GeV^2 it exceeds even the photoproduction value. At larger $|t|$ the electroproduction data are below the photoproduction band and do not show the increase in R for $|t|>0.6$ GeV^2 as observed for $Q^2=0$.

The ratio R may be expressed in terms of the isoscalar A_s and isovector A_v amplitudes as

$$R=\frac{|A_v-A_s|^2}{|A_v+A_s|^2}.$$

Using the data of Fig. 27, we determine the sum

$$|A_v|^2+|A_s|^2=(1+R)\cdot\pi\cdot\frac{d^2\sigma(\pi^+ n)}{dtd\phi}$$

and the interference term

$$2|A_v|\cdot|A_s|\cdot\cos\alpha=(1-R)\cdot\pi\cdot\frac{d^2\sigma(\pi^+ n)}{dtd\phi}$$

where α is the phase angle between A_v and A_s. The results are plotted in Fig. 28. It is evident that at larger $|t|$ both amplitudes contribute significantly.

5.3.1. The quark model prediction of R and an estimate of the transverse $(\pi^- p)$ cross section. The quark model describes the π^+ and π^- production by photons in the s-channel according to the diagrams in Fig. 29. From these diagrams one expects a charge ratio of $R=1/4$, since the photon has to couple to an u quark to produce a π^+ and to a d quark for a π^-. The analogous u-channel diagrams predict of course a ratio of $R=4$. Barbour et al. [34] pointed out that the ratio $R\simeq 0.3$ observed in photoproduction at $0.2<|t|<0.8$ GeV^2 could be explained by the contribution of the diagrams in Fig. 29, since other contributions tend to cancel each other in this region of $|t|$.

One would naively expect incoherent photon quark interactions like the ones sketched in Fig. 29 to be more dominant at larger Q^2. Nachtmann [35] conjectured from a study of exclusive channels in deep inelastic lepton nucleon scattering within the framework of an extended quark-parton model a ratio R_U for the transverse part of the cross sections of

$$R_U=\frac{d\sigma_U(\pi^- p)}{dt}\Big/\frac{d\sigma_U(\pi^+ n)}{dt}=1/4.$$

The data on R shown in Fig. 27, which are close to 1/4 for $|t|>0.6$ GeV^2, support this prediction, since one would not expect a significant contribution of σ_L at larger $|t|$. It is therefore of great interest to determine the transverse cross section ratio at small $|t|$. To estimate $\sigma_U(\pi^- p)$ we make use of the fact that at high energies only unnatural parity exchange in the t-channel contributes to σ_L, σ_I, and $\sigma_{\|}$ (see Sect. 2). Of the relevant mesons π, A_1, and B only the B meson couples to the isoscalar component of the photon. Neglecting B meson exchange against the dominating π meson exchange yields σ_L, σ_I, and $\sigma_{\|}$ to be equal in both channels [8]. Comparison of Figs. 14 and 16 shows that this is in fact the case for σ_I. To determine $\sigma_U(\pi^- p)$ numerically we average between the two possibilities:

$$2\sigma_U(\pi^- p)=[\{\sigma_U(\pi^- p)+\varepsilon\sigma_L(\pi^- p)\}-\varepsilon\sigma_L(\pi^+ p)]+\sigma_{\|}(\pi^+ n)-\sigma_P(\pi^- p).$$

Using this relation and the data of Figs. 14 and 16, we calculate the ratio R_U of the transverse cross sections σ_U. The results are shown in Fig. 30. The experimental uncertainties are large but the data indicate R_U at $Q^2 = 0.70\ \text{GeV}^2$ to be smaller than in photoproduction [36].

5.4. $(K^+\Lambda)$ and $(K^+\Sigma^0)$ Production

A summary of the $(K^+\Lambda)$ and $(K^+\Sigma^0)$ data is shown in Fig. 31, where the cross section $2\pi \frac{d^2\sigma}{dtd\phi}$ averaged between $120° \leqq \phi \leqq 240°$ is plotted versus Q^2 for several t bins. Comparing these data with the $(\pi^+ n)$ data of Fig. 13, we find the K^+ cross section to be smaller by almost an order of magnitude at low $|t|$. Contrary to the $(\pi^+ n)$ channel, the K^+ cross section does not show any significant increase with Q^2 which would be expected if σ_L contributed strongly. The Q^2-dependence of the $(K^+\Lambda)$ cross section at fixed t is similar to the one of the total cross section, whereas the $(K^+\Sigma^0)$ production drops, at least at low $|t|$, considerably faster with increasing Q^2, We discuss this difference further in Sect. 5.4.1.

Figures 32 and 33 show the cross section $2\pi \frac{d^2\sigma}{dtd\phi}$ versus t. Results from several photo- [37–39] and electroproduction [40, 41] measurements are shown for comparison. The different data sets were again scaled in W according to $(W^2 - M^2)^{-2}$. The various experiments agree within their rather large uncertainties, except for the photoproduction data of [37] and [39]. At $|t| > 0.1\ \text{GeV}^2$ the data fall smoothly with increasing $|t|$, roughly like $e^{-2.1|t|}$ for the $(K^+\Lambda)$ and like $e^{-1.0|t|}$ for the $(K^+\Sigma^0)$.

The cross section components $\sigma_U + \varepsilon\sigma_L$, σ_P, and σ_I are shown in Figs. 34 and 35 together with the results from [40] and [41]. Our results are in good agreement with those from the Harvard-Cornell group [40]. The cross section $\sigma_U + \varepsilon\sigma_L$ for the $(K^+\Lambda)$ channel dominates for $|t| \lesssim 0.5\ \text{GeV}^2$. σ_I and σ_P being small implies $\sigma_\perp \simeq \sigma_\parallel$. For the $(K^+\Sigma^0)$ channel however, σ_P is negative indicating $\sigma_\perp > \sigma_\parallel$. In photoproduction $\sigma_\perp$ and $\sigma_\parallel$ were separated only for the sum of $(K^+\Lambda)$ and $(K^+\Sigma^0)$ for which $\sigma_\perp \gg \sigma_\parallel$ was found [42]. The large value of $|\sigma_P|$ allows the estimation of an upper limit of σ_L for the $(K^+\Sigma^0)$ final state, using the inequality [17]

$$\frac{\sigma_L}{\sigma_U} \leqq \frac{1}{\varepsilon} \frac{(\sigma_U + \varepsilon\sigma_L) - |\sigma_P|}{\sigma_U} \leqq \frac{1}{\varepsilon}\left(\frac{\sigma_U + \varepsilon\sigma_L}{|\sigma_P|} - 1\right).$$

The results are listed in Table 13. So far the only attempt to separate σ_L and σ_U for K^+ electroproduction was made by the Harvard-Cornell collaboration [43];

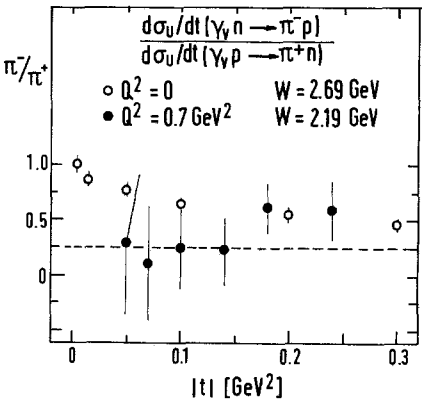

Fig. 30. The π^-/π^+ ratio for the transverse cross section (see text). The photoproduction measurements are from [36]

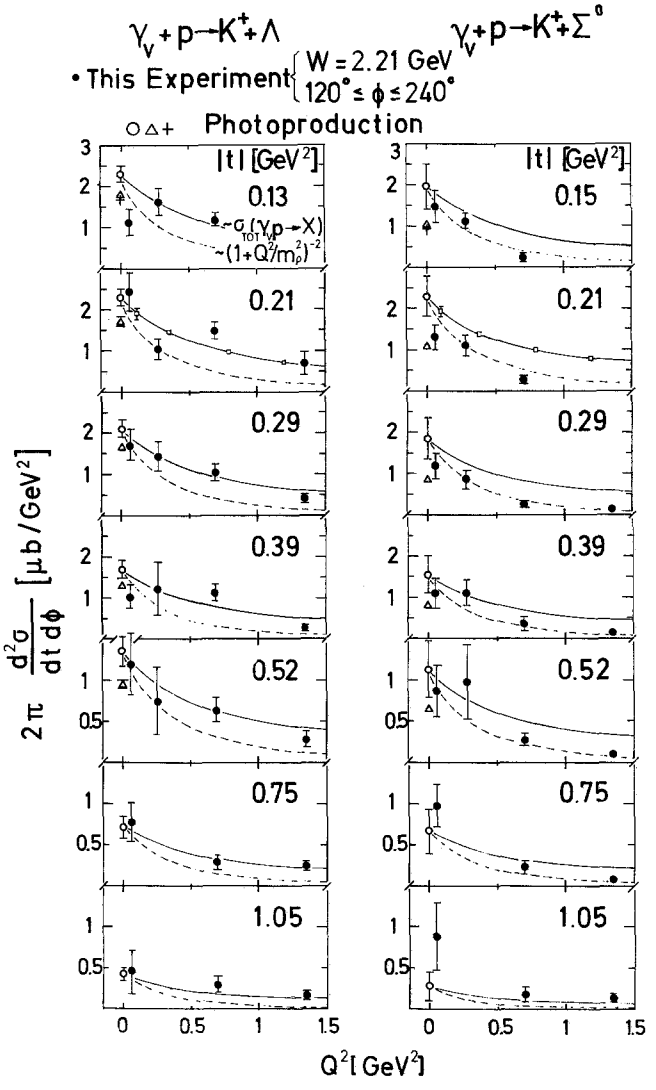

Fig. 31. The Q^2-dependence of the $(K^+\Lambda)$ and $K^+\Sigma^0)$ cross sections $2\pi d^2\sigma/dtd\phi$. The photoproduction data are from [37, 38, 39]. The full line is proportional to $\sigma_{\text{tot}}(\gamma_v p)$, the dashed line to $(1 + Q^2/m_\rho^2)^{-2}$

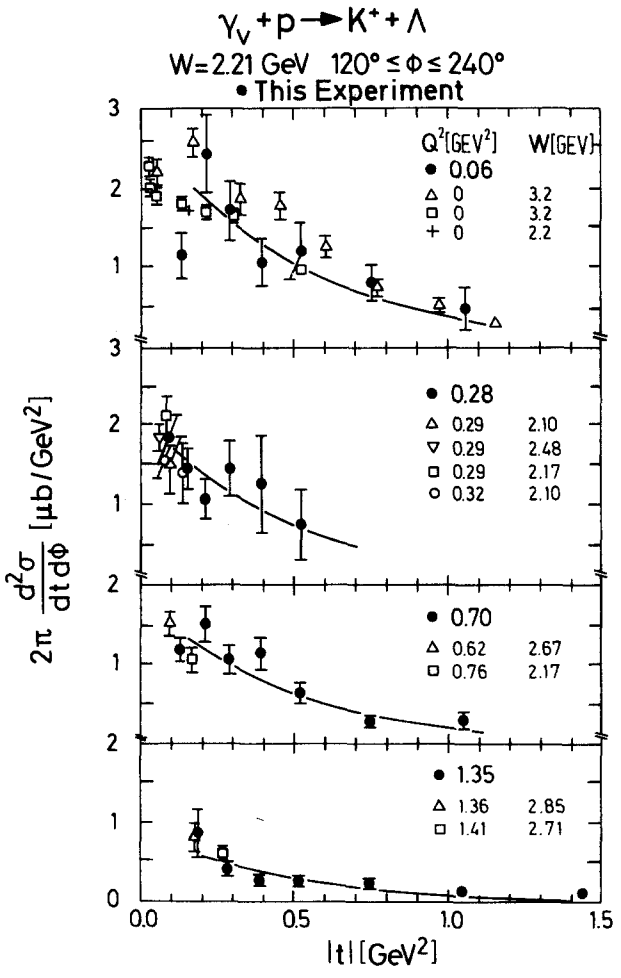

Fig. 32. The t-dependence of the $(K^+\Lambda)$ cross section $2\pi d^2\sigma/dtd\phi$. The other data [37–41] are scaled in W. The curves are proportional to exp $(2.1\,t)$

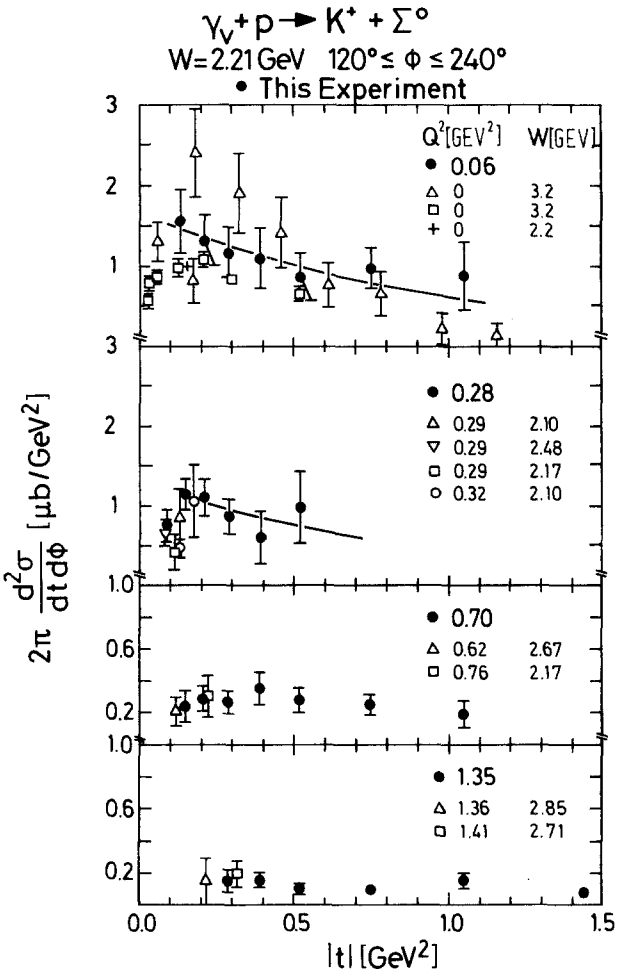

Fig. 33. The t-dependence of the $(K^+\Sigma^0)$ cross section $2\pi d^2\sigma/dtd\phi$. The other data [37–41] are scaled in W. The curves are proportional to exp $(1.0\,t)$

Table 13a. Upper limits L^Σ for σ_L and R^Σ for σ_L/σ_U for the $(K^+\Sigma^0)$ channel (see text), $W=2.21$ GeV

Q^2 (GeV²)	$\lvert t\rvert$ (GeV²)	L^Σ (μb/GeV²)	R^Σ (integrated over t)
	0.14	0.36 ± 0.15	
0.70	0.21	0.21 ± 0.11	1.82 ± 1.44
	0.29	0.22 ± 0.11	
	0.29	0.08 ± 0.11	
1.35	0.39	0.03 ± 0.12	0.28 ± 0.28
	0.52	-0.01 ± 0.09	

Table 13b. The ratio σ_L/σ_U [43], $Q^2=1.19$ GeV², $W=2.14$ GeV

	$\lvert t\rvert$ (GeV²)	σ_L/σ_U
$K^+\Sigma^0$	0.33 – 0.38	$-0.14^{+1.56}_{-0.61}$
$K^+\Lambda$	0.25 – 0.30	$1.10^{+0.94}_{-0.60}$

their results are included in Table 13 as well. For a detailed discussion of K^+ electroproduction in terms of Regge models we refer to [44].

5.4.1. The Σ^0/Λ ratio and the quark model prediction. It has been known for some time that the $(K^+\Sigma^0)$ cross section decreases faster with increasing Q^2 than the $(K^+\Lambda)$ cross section. Two possible explanations for this have been suggested: The first assumes that only the $(K^+\Lambda)$-channel has a sizeable longitudinal cross section, since the main contribution to σ_L is expected from K exchange and since the coupling constant $g^2_{pK\Lambda} \gg g^2_{pK\Sigma^0}$. However there is no experimental evidence for σ_L dominating the $(K^+\Lambda)$-channel. The second explanation is based on the quark-parton model. Measurements of the ratio of the neutron and proton structure functions [47] show that $\nu W_2^N/\nu W_2^P \to 1/4$ as $x=Q^2/2M\nu \to 1$. This implies that the remaining part of the nucleon is in an $I=0$ state when a photon

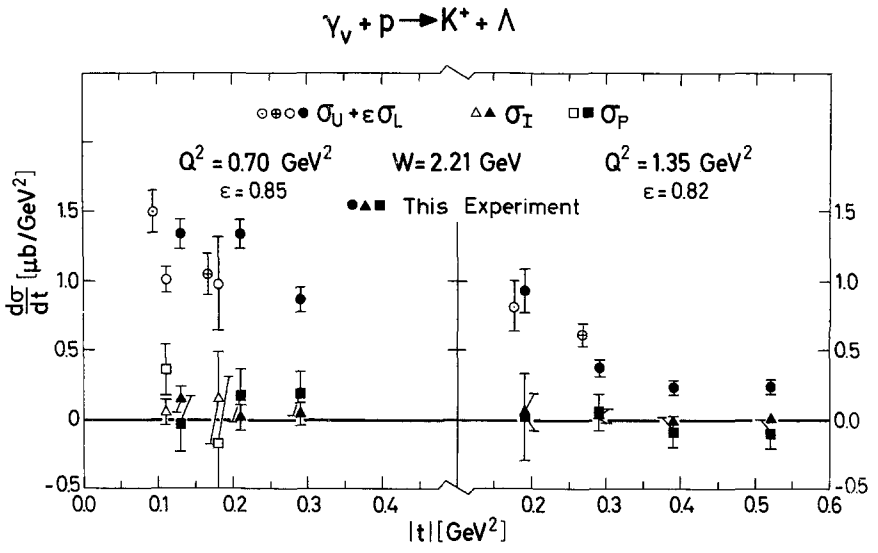

Fig. 34. The $(K^+\Lambda)$ cross section components. The other data (open symbols, $Q^2 = 0.53$ GeV^2 [41], remaining symbols $Q^2 = 0.62$, 0.76, 1.36, 1.41 GeV^2 [40]) are scaled in W

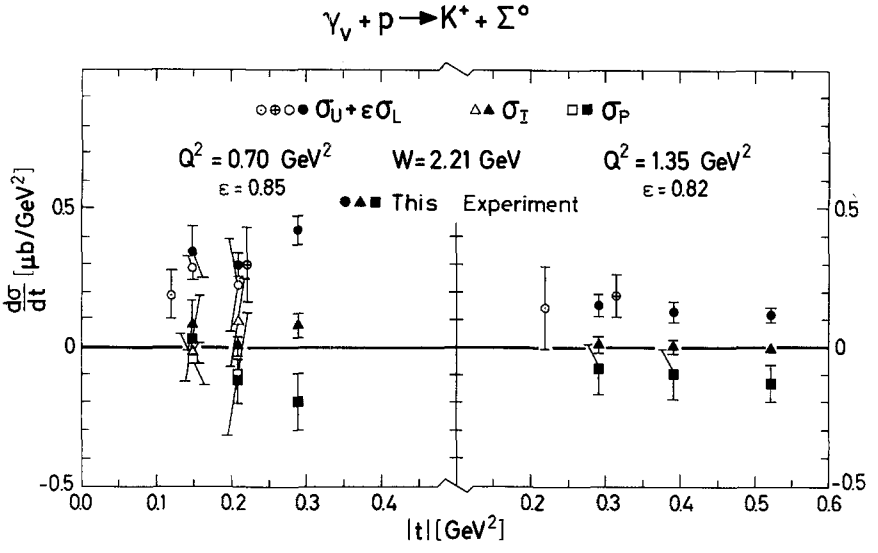

Fig. 35. The $(K^+\Sigma^0)$ cross section components. The references are the same as in Fig. 34

interacts with a quark at $x=1$. The production of a Λ is therefore favoured against the production of a Σ^0. Nachtmann [45] as well as Cleymans and Close [46] pursued these arguments further. In Fig. 36 we show the prediction for the upper and lower limit of the ratio of transverse cross sections obtained from [45]. These limits were determined by minimum and maximum estimates of the strange quark contributions from the sea. The results of our experiment and data from photoproduction [47], close in W and t to our data, are shown in Fig. 36 as well. The data are in reasonable agreement with the theoretical prediction.

6. Summary and Conclusions

In this experiment we studied a few virtual photon induced reaction channels in some detail hoping for insight into the mechanism which produces the scaling behaviour of the total electroproduction cross section. In the following we summarize the main results:

1. For $|t| \leqq 0.2$ GeV^2 $(\pi^+ n)$ electroproduction shows a large longitudinal cross section. This σ_L as well as the transverse cross sections $\sigma_{\|}$, $\sigma_{\perp}$ and the transverse-longitudinal interference contribution σ_I can be described by a modified Born term model which

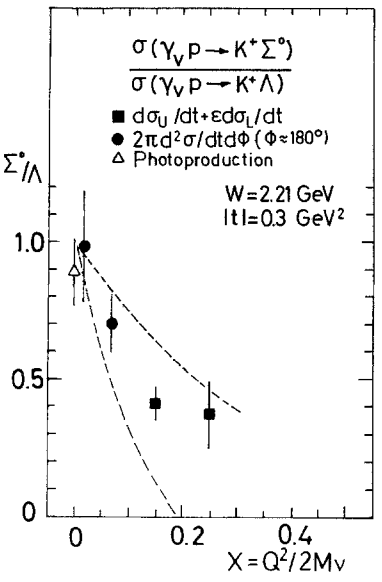

Fig. 36. The ratio of the $(K^+\Sigma^0)$ to the $(K^+\Lambda)$ cross section. The photoproduction point is taken from [37]. The curves show the limits given by the quark-parton model [45]

treats the off shell nucleon form factors as a free parameter. In this model σ_L is given by the one-pion exchange term and therefore allows the determination of the pion electromagnetic form factor. The result is $F_\pi(Q^2=0.7\ \text{GeV}^2)=0.42\pm0.015$ which is in good agreement with the isovector Dirac form factor of the nucleon.

2. At low $|t|$ the transverse cross section $\frac{d\sigma_U(\pi^+ n)}{dt}$ drops steeply from its photoproduction value to $Q^2\simeq 0.5$ GeV^2 and the stays constant independent of Q^2. This follows from a comparison of our data with those on photo- and electroproduction by the Harvard-Cornell and another DESY group.
3. The steep decrease of $\frac{d\sigma_U(\pi^+ n)}{dt}$ with Q^2 becomes less pronounced with increasing $|t|$. For $|t|\geqq 0.8$ GeV^2 the cross section $d^2\sigma/dtd\phi$ hardly shows any Q^2 dependence. The cross section $\sigma(\pi^+ n)$ which was obtained by integration of our and the Harvard-Cornell data on $d\sigma/dt$ exhibits the same Q^2-dependence as the total electroproduction cross section $\sigma_{tot}(\gamma_v p)$ for $Q^2\geqq 0.28$ GeV^2. The Q^2-dependence of $\sigma(\pi^+ n)$ arises mainly from the variation of $|t|_{min}$. The quantity $Q^6\cdot\sigma(\pi^+ n)$ scales in ω' and follows roughly the prediction based on correspondence arguments by Bjorken and Kogut.
4. At large $|t|$ the $(\pi^- p)$ cross section is significantly smaller than the $(\pi^+ n)$ cross section. For $|t|\geqq 0.6$ GeV^2 the ratio $R=\sigma(\pi^- p)/\sigma(\pi^+ n)$ is lower than in photoproduction and close to 1/4. At low $|t|$ we find $R\simeq 1$, due to the dominance of σ_L. The data however indicate that the ratio of the transverse cross sections σ_U is also at low $|t|$ smaller than in photoproduction.
5. The $(K^+\Lambda)$ cross section shows at fixed t a Q^2-dependence similar to $\sigma_{tot}(\gamma_v p)$, whereas the $(K^+\Sigma^0)$ cross section decreases much faster with Q^2. The ratio $\sigma(K^+\Sigma^0)/\sigma(K^+\Lambda)$ agrees with the quark model prediction.

The findings 2–5 seem to support the ideas of the quark-parton model. One would naively expect some coherent interaction peaking at low $|t|$ which would decrease with Q^2 more strongly than the incoherent quark-parton interaction. The results 2 and 3 support this picture; the cross section $d\sigma_U/dt$ decreases at low $|t|$ steeply with Q^2 and remains then independent of Q^2. Qualitatively similar effects were observed for the reaction $\gamma_v + p\to\pi^0 + p$ [48]. The result 4 is evident from naive charge counting rules and has been predicted by more refined calculations. The (Σ^0/Λ) ratio has been regarded for some time as evidence of the quark-parton model.

Acknowledgement. We want to thank Dr. J. Körner and Prof. G. Weber for the reading of the manuscript and together with Profs. F. Gutbrod and G. Kramer for helpful discussions. We acknowledge the work of the floor service, synchrotron and computer groups. We enjoyed the wholehearted support of Mr. K. Fesefeld, Mr. H. Grote, Mr. G. Guzielski, Miss C. Lamberts, and Mr. P. Warming. We also want to thank our technicians Mr. J. Bech, Miss A. Dreher, Mr. P. Lüthke, Mr. V. Masbender, and Miss B. Nack for their assistance during the setup and running of the experiment and Mrs. S. Platz for carefully typing the manuscripts.

References

1. P. Brauel et al.: Phys. Lett. **65B**, 181 (1976)
2. P. Brauel et al.: Phys. Lett. **65B**, 184 (1976)
3. P. Brauel et al.: Phys. Lett. **69B**, 253 (1977)
4. K. Berkelmann: Proc. Int. Symp. on Electron and Photon Interactions at High Energies, Ithaca, N.Y. (1971)
5. C. Driver et al.: Phys. Lett. **35B**, 77 (1971); Nucl. Phys. B**30**, 245 (1971); C. N. Brown et al.: Phys. Rev. Lett. **26**, 987, 991 (1971); Phys. Rev. D**8**, 92 (1973); Phys. Rev. D**9**, 1229 (1974); P. S. Kummer et al.: Lett. Nuovo Cimento **1**, 1026 (1971); Nucl. Phys. B**42**, 369 (1972)
6. F. Gutbrod, G. Kramer: Nucl. Phys. B**49**, 461 (1972); F. A. Berends: Phys. Rev. D**1**, 2590 (1970)
7. R. C. E. Devenish, D. H. Lyth: Phys. Rev. D**5**, 47 (1972)
8. G. Kramer: Acta Phys. Austriaca **40**, 150 (1974)
9. A. Bartl, P. Urban: Acta Phys. Austriaca **24**, 139 (1966); L. W. Mo, Y. S. Tsai: Rev. Modern Phys. **41**, 205 (1969)
10. For more details see M. Helm: Thesis (1978). Internal Report DESY F22-78/03
11. For more details see Th. Canzler: Thesis (1977). Internal Report DESY F22-77/01
12. For more details see M. Schädlich: Thesis (1976). Internal Report DESY F22-76/02
13. B. Richter: Proc. 14th Int. Conf. High Energy Physics. Vienna (1968)

14. P. Heide et al.: Phys. Rev. Lett. **21**, 248 (1968)
15. A. M. Boyarski et al.: Phys. Rev. Lett. **21**, 1167 (1968)
16. C. J. Bebek et al.: Phys. Rev. D**13**, 25 (1976)
17. For more details see P. Brauel: Thesis (1978). Internal Report DESY F22-78/04
18. G. Buschhorn et al.: Phys. Rev. Lett. **17**, 1027 (1966); Phys. Rev. Lett. **18**, 571 (1967)
19. Z. Bar-Yam et al.: Phys. Rev. Lett. **19**, 40 (1967)
20. C. Geweniger et al.: Phys. Lett. **29**B, 41 (1969)
21. H. Ackermann et al.: Nucl. Phys. B**137**, 294 (1978)
22. C. J. Bebek et al.: Phys. Rev. D**17**, 1693 (1978)
23. C. J. Bebek et al.: Phys. Rev. Lett. **37**, 1326 (1976)
24. K. Lübelsmeyer: Proc. 4th Int. Symp. on Electron and Photon Interactions at High Energies, Liverpool (1969)
25. P. Joos: Compilation of photoproduction data above 1.2 GeV, DESY-HERA 70-1
26. C. J. Bebek et al.: Phys. Rev. D**9**, 1229 (1974)
27. S. D. Holmes et al.: Phys. Rev. Lett. **35**, 1313 (1975)
28. R. L. Anderson et al.: Phys. Rev. D**14**, 679 (1976)
29. H. Meyer et al.: Phys. Lett. B**33**, 189 (1970)
30. F. W. Brasse et al.: Nucl. Phys. B**39**, 421 (1972)
31. J. D. Bjorken, J. Kogut: Phys. Rev. D**8**, 1341 (1973)
32. F. J. Gilman: Phys. Rev. **167**, 1365 (1968)
33. L. N. Hand: Phys. Rev. **129**, 1834 (1963)
34. I. Barbour et al.: Phys. Rev. D**4**, 1521 (1971)
35. O. Nachtmann: Nucl. Phys. B**115**, 61 (1976)
36. C. Geweniger: Thesis (1972). Internal Report DESY F35-72/2
37. A. M. Boyarski et al.: Phys. Rev. Lett. **22**, 1131 (1969)
38. P. Feller et al.: Nucl. Phys. B**39**, 413 (1972)
39. H. Burfeindt et al.: Contribution to the 6th Int. Symp. on Electron and Photon Interaction at High Energies. Bonn (1973)
40. C. J. Bebek et al.: Phys. Rev. D**15**, 594 (1977)
41. T. Azemoon et al.: DESY-report 74/75 (1974)
42. D. J. Quinn et al.: Phys. Rev. Lett. **34**, 543 (1975)
43. C. J. Bebek et al.: Phys. Rev. D**15**, 3082 (1977)
44. A. Bartl, W. Majerotto: Nucl. Phys. B**90**, 285 (1975)
45. O. Nachtmann: Nucl. Phys. B**74**, 422 (1974)
46. J. Cleymans, F. E. Close: Nucl. Phys. B**85**, 429 (1975)
47. A. Bodek et al.: Phys. Lett. **51**B, 417 (1974)
48. F. W. Brasse et al.: Phys. Lett. **58**B, 467 (1975)